

The Monitor project: rotation of low-mass stars in the open cluster M34

Jonathan Irwin,^{1*} Suzanne Aigrain,¹ Simon Hodgkin,¹ Mike Irwin,¹ Jerome Bouvier,² Cathie Clarke,¹ Leslie Hebb³ and Estelle Moraux²

¹*Institute of Astronomy, University of Cambridge, Madingley Road, Cambridge CB3 0HA*

²*Laboratoire d'Astrophysique, Observatoire de Grenoble, BP 53, F-38041 Grenoble Cédex 9, France*

³*School of Physics and Astronomy, University of St Andrews, North Haugh, St Andrews KY16 9SS*

Accepted 2006 May 5. Received 2006 May 5; in original form 2006 April 18

ABSTRACT

We report on the results of a V - and i -band time-series photometric survey of M34 (NGC 1039) using the Wide Field Camera (WFC) on the Isaac Newton Telescope (INT), achieving better than 1 per cent precision per data point for $13 \lesssim i \lesssim 17$. Candidate cluster members were selected from a V versus $V - I$ colour–magnitude diagram over $14 < V < 24$ ($0.12 \lesssim M/M_{\odot} \lesssim 1.0$), finding 714 candidates, of which we expect ~ 400 to be real cluster members (taking into account contamination from the field). The mass function was computed, and found to be consistent with a lognormal distribution in $dN/d \log M$. Searching for periodic variable objects in the candidate members gave 105 detections over the mass range $0.25 < M/M_{\odot} < 1.0$. The distribution of rotation periods for $0.4 < M/M_{\odot} < 1.0$ was found to peak at ~ 7 d, with a tail of fast rotators down to periods of ~ 0.8 d. For $0.25 < M/M_{\odot} < 0.4$ we found a peak at short periods, with a lack of slow rotators (e.g. $P \gtrsim 5$ d), consistent with the work of other authors at very low masses. Our results are interpreted in the context of previous work, finding that we reproduce the same general features in the rotational period distributions. A number of rapid rotators were found with velocities \sim a factor of 2 lower than in the Pleiades, consistent with models of angular momentum evolution assuming solid body rotation without needing to invoke core–envelope decoupling.

Key words: techniques: photometric – surveys – stars: rotation – open clusters and associations: individual: M34.

1 INTRODUCTION

M34 (NGC 1039) is a relatively well-studied intermediate-age open cluster (~ 200 Myr; Meynet, Mermillod & Maeder 1993; Jones & Prosser 1996), at a distance of ~ 470 pc, distance modulus $(M - m)_0 = 8.38$ (Jones & Prosser 1996), with low reddening: $E(B - V) = 0.07$ mag (Canterna, Crawford & Perry 1979). The cluster is located at $\alpha = 2^{\text{h}}42^{\text{m}}06^{\text{s}}$, $\delta = +42^{\circ}46'$ (J2000 coordinates from SIMBAD), corresponding to Galactic coordinates $l = 143^{\circ}7$, $b = -15^{\circ}6$.

Clusters in the age range between α Persei (~ 80 Myr; Stauffer et al. 1999) and the Hyades (~ 625 Myr; Perryman et al. 1998) are important for constraining stellar evolution models. A $1 M_{\odot}$ star reaches the zero-age main-sequence (ZAMS) at ~ 30 Myr, with progressively later spectral types reaching the ZAMS at later times. M34 is useful in this context owing to both its age and relative proximity, where we can study solar mass stars after evolving for a short time on the main sequence, and lower-mass stars as they finish

pre-main-sequence evolution. We estimate that $0.5 M_{\odot}$ stars reach the ZAMS at approximately the age of M34, using the models of Baraffe et al. (1998).

Membership surveys of M34 using proper motions (Ianna & Schlemmer 1993; Jones & Prosser 1996) have been carried out using photographic plates down to $V \sim 16.2$ ($M \sim 0.7 M_{\odot}$), finding a mean cluster proper motion of ~ 20 mas yr $^{-1}$. Studies of M34 members in the literature include spectroscopic abundance measurements for G and K dwarfs, finding a mean cluster metallicity $[\text{Fe}/\text{H}] = +0.07 \pm 0.04$ (Schuler et al. 2003). Rotation studies have used both spectroscopy (Soderblom, Jones & Fischer 2001), covering the high- to intermediate-mass end of the M34 cluster members, down to G spectral types, and photometry (Barnes 2003). Finally, a *ROSAT* soft X-ray survey (Simon 2000), detected 32 sources.

The existing surveys in M34 have concentrated on the high-mass end of the cluster sequence (typically K or earlier spectral types). Later spectral types, in particular M, down to the substellar regime, are not well studied. A catalogue of low-mass M34 members could be used to perform both photometric (e.g. surveys for rotation and eclipses) and spectroscopic (e.g. spectral typing and metal abundance) studies of the K and M dwarf populations.

*E-mail: jmi@ast.cam.ac.uk

1.1 Evolution of stellar angular momentum

The early angular momentum distribution of young stars is commonly explained as resulting from an initial intrinsic angular momentum distribution consisting of relatively mild rotators (e.g. with rotational periods of ~ 8 d for typical very young classical T-Tauri stars such as the population of slow rotators in the Orion nebula cluster (ONC), Herbst et al. 2002), modified by subsequent spin-up of the star during contraction on the pre-main sequence (PMS). Observations indicate that a fraction of the stars spin slower than expected due to contraction, suggesting that they are prevented from spinning up. The most popular explanation for this is disc locking (e.g. Königl 1991; Collier Cameron, Campbell & Quaintrell 1995; Bouvier, Forestini & Allain 1997). In the T-Tauri phase, stars are still surrounded by accretion discs, so a star could retain a constant rotation rate during contraction due to angular momentum transport via magnetic interaction of the star and disc. The stars are thus prevented from spinning up until the accretion disc dissolves. Recent evidence in favour of this hypothesis has been obtained from *Spitzer* studies, e.g. Rebull et al. (2006).

Very young clusters such as the ONC (age $\sim 1 \pm 1$ Myr; Hillenbrand 1997) provide an ideal testing ground for these models. Herbst et al. (2002) found a bimodal period distribution in this cluster for $M > 0.25 M_{\odot}$, with short- and long-period peaks, where the long-period peak corresponds to stars which are still locked to their circumstellar discs, preventing spin-up, whereas the stars comprising the short-period peak have had time to spin-up since becoming unlocked from their discs. The distribution appeared to be unimodal at low masses ($M < 0.25 M_{\odot}$) with only a short-period peak, implying that all of the low-mass stars were fast rotators and presumably not disc locked.

After the accretion discs dissolve (by 20 Myr for 90 per cent of stars; see also Haisch, Lada & Lada 2001), the stars are free to spin up as they contract on the PMS. During this phase of the evolution, the stellar contraction dominates the angular momentum distribution. Disc lifetimes can be constrained by examining the rotation period distributions in this age range.

As the stars approach the ZAMS (at ~ 30 – 100 Myr for G and K spectral types), the contraction rate slows, and angular momentum losses begin to dominate. These are thought to result from magnetized stellar winds (Weber & Davis 1967) and cause the stars to spin down gradually on the main sequence. Previous studies (e.g. see Stassun & Terndrup 2003, for a recent review) have shown that most stars in young clusters (~ 100 Myr) rotate slowly ($v \sin i < 20 \text{ km s}^{-1}$), but a minority rotate much faster ($v \sin i \sim 200 \text{ km s}^{-1}$ for the fastest rotators). Moving to older clusters such as the Hyades (~ 625 Myr; Perryman et al. 1998), nearly all of the velocities of G and K stars have fallen to $\lesssim 10 \text{ km s}^{-1}$. This process must have occurred over the age range (~ 200 Myr) in which M34 lies.

The observations indicate that there is a large convergence in rotation rate from the Pleiades (~ 125 Myr; Stauffer, Schultz & Kirkpatrick 1998) to the Hyades, but with little change for the slowest rotators. The change in rotation rate is also found to be mass dependent, in the sense that lower-mass stars require lower angular momentum loss rates in order to reproduce the observations (Barnes & Sofia 1996). In terms of the models, assuming solid body rotation, in the simplest Skumanich (1972) model the angular momentum evolves as the $-1/2$ power of the age t of the star. This does not reproduce the observed convergence in rotation rates, or the mass dependence. Furthermore, the observations appear to require a steeper early evolution than $t^{-1/2}$, followed by a flattening at later times.

Core–envelope decoupling (e.g. Soderblom et al. 1993b) has been invoked to explain these observations. In the core–envelope decoupling scenario, the stars undergo differential rotation. While the core is decoupled from the envelope, all the angular momentum that is lost to the outside is taken from the envelope only. This rapidly spins down the surface layers, giving rise to the observed steep early evolution, while the core retains a high rotation rate. Later, as the core and envelope are gradually recoupled, the core effectively acts as a reservoir of angular momentum, giving rise to the observed flattening of the rotational evolution. These models are constrained by the situation in the sun, which is approximately a solid body rotator, i.e. no differential rotation, so the decoupling must evolve out (see also Eff-Darwich, Korzennik & Jiménez-Reyes 2002 and references therein).

Results from more comprehensive models assuming solid body rotation are now able to provide an alternative explanation for the observations. For example, in the models of Bouvier et al. (1997), the more rapid spin-down of faster rotators (and hence convergence in rotation rates) can be explained in terms of their adopted angular momentum loss law, without requiring core–envelope decoupling, and the longer spin-down time-scale for low-mass stars is explained by mass-dependent saturation of the angular momentum losses. In the $\alpha - \omega$ dynamo model, the mass dependency is a natural consequence of assuming that the saturation in angular momentum losses results from saturation of the dynamo itself. Alternatively, Giampapa et al. (1996) have suggested that fully convective stars have complex magnetic field geometries, mostly consisting of small loops contributing little to angular momentum losses. The change in magnetic field geometry toward lower-mass stars, with more closed loops, could then also give rise to a mass-dependent saturation of the angular momentum losses.

A review of these ideas is given in Bouvier (1997), based on the results of $v \sin i$ measurements in a number of open clusters, including α Persei, the Pleiades and the Hyades.

Recent work has been carried out at lower masses, e.g. Scholz & Eislöffel (2004), who measured rotation periods for nine very low-mass (VLM) Pleiades members with $0.08 < M/M_{\odot} < 0.25$. They found a lack of slow rotators, with observed rotation periods from ~ 0.012 – 1.7 d, tending to increase linearly with mass. The implications of these results are that any angular momentum loss experienced by VLM stars must be very small, to preserve the high rotation velocities, or equivalently, the braking time-scale of VLM stars is longer than that of higher-mass stars. These results lend weight to the idea that angular momentum loss is a strong function of stellar mass, and weakens towards the VLM regime (e.g. Krishnamurthi et al. 1997 for solar mass stars and Bouvier et al. 1997).

Mid- to low-mass stars ($0.4 \lesssim M/M_{\odot} \lesssim 1.0$) in intermediate-age clusters such as M34 have experienced a period of evolution after the PMS spin-up, and are thus ideal for constraining spin-down time-scales on the early main sequence. At very low mass, we can also examine the late PMS angular momentum evolution.

1.2 The survey

We have undertaken a photometric survey in M34 using the Isaac Newton Telescope (INT). Our goals are threefold: first, to establish a catalogue of candidate low-mass M34 members; secondly, to study rotation periods in a sample of these low-mass members and thirdly, to look for eclipsing binary systems containing low-mass stars, to obtain dynamical mass measurements in conjunction with radial velocities (RVs) from follow-up spectroscopy. Such systems provide the most accurate determinations of fundamental stellar parameters

(in particular, masses) for input to models of stellar evolution, which are poorly constrained in this age range. We defer discussion of our eclipsing binary candidates to a later paper once we have obtained suitable follow-up spectroscopy.

These observations are part of a larger photometric monitoring survey of young open clusters over a range of ages and metallicities (the Monitor project, Hodgkin et al. 2006 and Aigrain et al. in preparation).

The remainder of the paper is structured as follows: the observations and data reduction are described in Section 2, and the colour-magnitude diagram (CMD) of the cluster and candidate membership selection are presented in Section 3. The method we use for obtaining photometric periods is presented in Section 4, and the resulting rotation periods and amplitudes are discussed in Section 5. Finally, we summarize our conclusions in Section 6.

2 OBSERVATIONS AND DATA REDUCTION

Photometric monitoring data were obtained using the 2.5 m INT, with the Wide Field Camera (WFC) during a 10-night observing run in 2004 November. This instrument provides a field of view (FOV) of approximately 34×34 arcmin² at the prime focus of the INT, over a mosaic of four 2×4 k pixel CCDs, with ~ 0.33 arcsec pixels. Our primary target was the ONC, which was observable for only half the night from La Palma, so the first ~ 4.5 h of each night were used to observe M34.

Monitoring was carried out using alternating 60-s *V*-band and 30-s *i*-band exposures, giving an observing cadence of ~ 3.5 min, over a ~ 0.3 -deg² region of the cluster. We also obtained $\sim 2 \times 300$ s $H\alpha$ exposures per night. Data were obtained on a total of eight out of the 10 nights (many of these were partial due to poor weather), giving 275 *V*-band and 268 *i*-band frames after rejection of observations influenced by technical problems (image trailing), and 6 $H\alpha$ frames. Our observations are sufficient to give an rms per data point of 1 per cent or better down to $i \sim 17$, with saturation at $i \sim 13$ (see Fig. 1), corresponding to a range of spectral types for M34 members from mid-G to early-M.

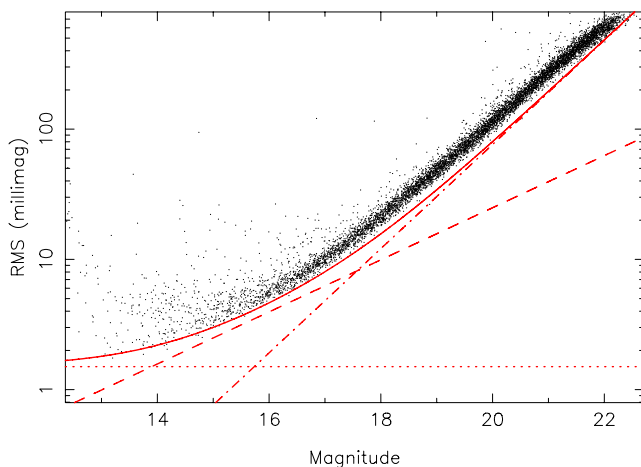


Figure 1. Plot of rms scatter per data point as a function of magnitude for the *i*-band observations of M34, for all unblended objects with stellar morphological classifications. The diagonal dashed line shows the expected rms from Poisson noise in the object, the diagonal dot-dashed line shows the rms from sky noise in the photometric aperture, and the dotted line shows an additional 1.5 mmag contribution added in quadrature to account for systematic effects. The solid line shows the overall predicted rms, combining these contributions.

For a full description of our data reduction steps, the reader is referred to Irwin et al. (in preparation). Briefly, we used the pipeline for the INT wide-field survey (Irwin & Lewis 2001) for 2D instrumental signature removal (cross-talk correction, bias correction, flat-fielding, defringing) and astrometric and photometric calibration. We then generated the *master catalogue* for each filter by stacking 20 of the frames taken in the best conditions (seeing, sky brightness and transparency) and running the source detection software on the stacked image. The resulting source positions were used to perform aperture photometry on all of the time-series images. We achieved a per data point photometric precision of ~ 2 – 5 mmag for the brightest objects, with rms scatter < 1 per cent for $i \lesssim 17$ (see Fig. 1), corresponding to ~ 1100 unblended stars.

Our source detection software flags as likely blends any objects detected as having overlapping isophotes. This information is used, in conjunction with a morphological image classification flag also generated by the pipeline software (Irwin & Lewis 2001) to allow us to identify non-stellar or blended objects in the time-series photometry.

Photometric calibration of our data was carried out using regular observations of Landolt (1992) equatorial standard star fields in the usual way. This is not strictly necessary for the purely differential part of a campaign such as ours, but the cost of the extra telescope time for the standards observations is negligible, for the benefits of providing well-calibrated photometry (e.g. for the production of CMDs).

Light curves were extracted from the data for ~ 14000 objects, 8500 of which had stellar morphological classifications, using our standard aperture photometry techniques, described in Irwin et al. (in preparation). We fit a 2D quadratic polynomial to the residuals in each frame (measured for each object as the difference between its magnitude on the frame in question and the median calculated across all frames) as a function of position, for each of the four WFC CCDs separately. Subsequent removal of this function accounted for effects such as varying differential atmospheric extinction across each frame. Over a single WFC CCD, the spatially varying part of the correction remains small, typically ~ 0.02 mag peak-to-peak. The reasons for using this technique are discussed in more detail in Irwin et al. (in preparation).

For the production of deep CMDs, we stacked 120 observations in each of *V* and *i*, taken in good seeing and sky conditions (where possible, in photometric conditions). Since there were insufficient observations taken in truly photometric conditions, the stacked frames were corrected for the corresponding error in the object magnitudes by comparing to a reference frame in known photometric conditions, and using the common objects to place stacked frames on the correct zero-point system. The required corrections were typically $\lesssim 0.5$ mag. The limiting magnitudes, measured as the approximate magnitude at which our catalogues are 50 per cent complete,¹ on these images were $V \simeq 23.4$ and $i \simeq 22.6$. For $H\alpha$ we stacked all of the observations taken in sufficiently good conditions (four frames), giving a limiting magnitude of $H\alpha \simeq 21.7$.² A single 600-s *r*-band frame was also taken, with a limiting magnitude of $r \simeq 22.1$.

¹ These were measured by inserting simulated stars into each image, and measuring the completeness as the fraction of simulated stars detected, as a function of magnitude.

² The $H\alpha$ magnitudes in this paper are approximately equivalent to *r*-band magnitudes for a continuum source, and were calibrated by observing Landolt (1992) standard stars.

3 SELECTION OF CANDIDATE LOW-MASS MEMBERS

The first step in our survey is to identify the likely low-mass cluster members. The proper motion surveys discussed in Section 1 are not suitable because they become incomplete at the bright end of our magnitude range, e.g. $V \gtrsim 13$ assuming an apparent distance modulus to M34 of 8.60, estimated from fig. 8 of Jones & Prosser (1996). We have therefore used CMDs to search for candidate low-mass members in M34.

Since we only have optical photometry available over the whole mass range, the analysis here is preliminary and yields candidate cluster members only. We plan to make use of follow-up near-infrared (near-IR) observations and spectroscopy to improve the rejection of field stars, and will publish a more detailed membership survey of M34 in due course.

3.1 The V versus $V - I$ CMD

A V versus $V - I$ CMD of M34 was produced for selecting the candidate cluster members, and is shown in Fig. 2. The INT/WFC V and i measurements were converted to the Johnson–Cousins system of Landolt (1992) using colour equations derived from a large number of standard star observations, from the INT Wide Field Survey web pages³:

$$V - I = \frac{V_{\text{CCD}} - i_{\text{CCD}}}{0.894}, \quad (1)$$

$$V = V_{\text{CCD}} + 0.005 (V - I), \quad (2)$$

$$I = i_{\text{CCD}} - 0.101 (V - I). \quad (3)$$

Candidate cluster members were selected by defining an empirical main sequence. This was initially done ‘by eye’ and refined from the initial guess by computing an iterative $k\sigma$ clipped median in 1-mag bins of V magnitude, spaced at 0.5 mag, down the CMD from $V = 14$ to 24 (the range over which the main sequence was clearly defined on the diagram). The result is given in Table 1. A cut was defined by moving this line perpendicular to the mean gradient of the main sequence, toward the faint, blue end of the diagram, by $0.1 \text{ mag} + k\sigma(V - I)$ with $k = 2$, where $\sigma(V - I)$ is the photometric error in $V - I$. The resulting curve is shown in Fig. 2. The choice of k is somewhat arbitrary, and was made to give a good separation between cluster members and field stars. A greater main-sequence ‘width’ was allowed at the faint end to account for the increase in photometric errors.

Accepting all objects brighter and redder than the empirical main sequence ensures that multiple systems (e.g. binaries), which lie to this side of the main sequence, are not excluded. Examining the M34 CMD in Fig. 2 indicates that the additional contamination compared to applying a restrictive cut on the red side is not significant. Using the technique described, we found 714 candidate members.

We also considered using the model isochrone of Baraffe et al. (1998) for selecting candidate members. The model isochrone was found to be unsuitable due to the known discrepancy between the NextGen models and observations in the $V - I$ colour for $T_{\text{eff}} \lesssim 3700 \text{ K}$ (corresponding here to $V - I \gtrsim 2$). This was examined in more detail by Baraffe et al. (1998), and is due to a missing source of opacity at these temperatures, leading to overestimation of the V -band flux. Consequently, when we have used the NextGen

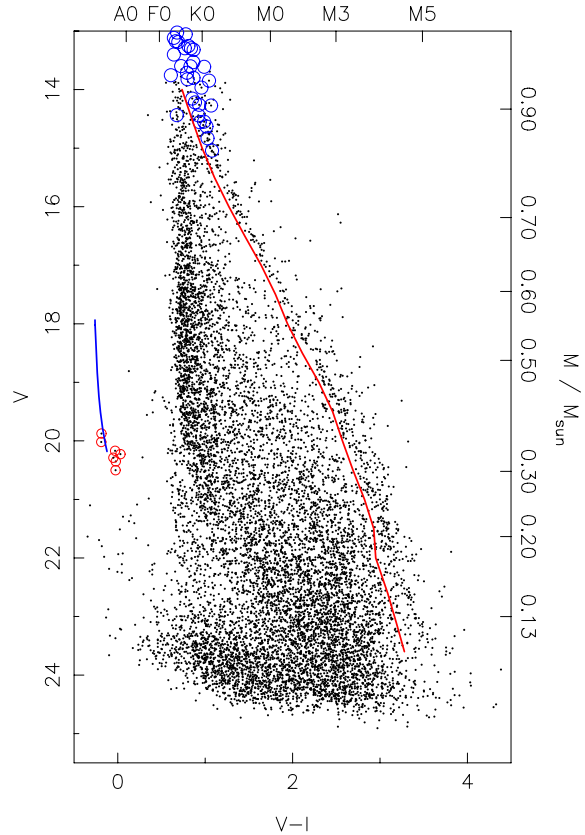


Figure 2. V versus $V - I$ CMD of M34 from stacked images, for all objects with stellar morphological classification. The cluster main sequence is clearly visible on the right-hand side of the diagram. The cut used to select candidate photometric members is shown as the solid line (all objects above and to the right-hand side were selected). The objects in our sample assigned membership probabilities $P > 80$ per cent by Jones & Prosser (1996) are shown as open circles. The mass scale is from the 200-Myr NextGen model isochrone (Baraffe et al. 1998), using our empirical isochrone to convert the V magnitudes to I magnitudes, and subsequently obtaining the masses from these, due to known problems with the V magnitudes from the models (see Section 3.1). The solid line and small circles at the lower left-hand side of the diagram show the models of Bergeron et al. (private communication) at the distance modulus of M34, for $\log g = 8.5$ to an age of 250 Myr, and our seven WD candidates (see Section 3.6).

isochrones to determine model masses and radii for our objects, the I -band absolute magnitudes were used to perform the relevant look-up, since these are less susceptible to the missing source of opacity, and hence give more robust estimates.

3.2 Completeness

The completeness of our source detection was estimated by inserting simulated stars as random x, y positions into our images, drawing the stellar magnitudes from a uniform distribution. Fig. 3 shows the resulting plot of completeness as a function of V -band magnitude. The completeness for objects on the M34 cluster sequence is close to 100 per cent up to the termination of the empirical main-sequence line at $V \sim 23$ ($I \sim 20$).

3.3 Contamination

In order to estimate the level of contamination in our catalogue, we used the Besançon galactic models (Robin et al. 2003) to generate

³ <http://www.ast.cam.ac.uk/~wfcSUR/>

Table 1. M34 empirical main sequence in dereddened $V - I$ colour and absolute V magnitude. These values were computed assuming a cluster reddening of $E(B - V) = 0.07$ and distance modulus $(M - m)_0 = 8.38$.

$(V - I)_0$	M_V
0.737	5.4
0.849	5.9
0.970	6.4
1.110	6.9
1.277	7.4
1.458	7.9
1.648	8.4
1.814	8.9
1.953	9.4
2.125	9.9
2.317	10.4
2.479	10.9
2.598	11.4
2.723	11.9
2.865	12.4
2.983	12.9
3.020	13.4
3.180	13.9
3.309	14.4
3.451	14.9

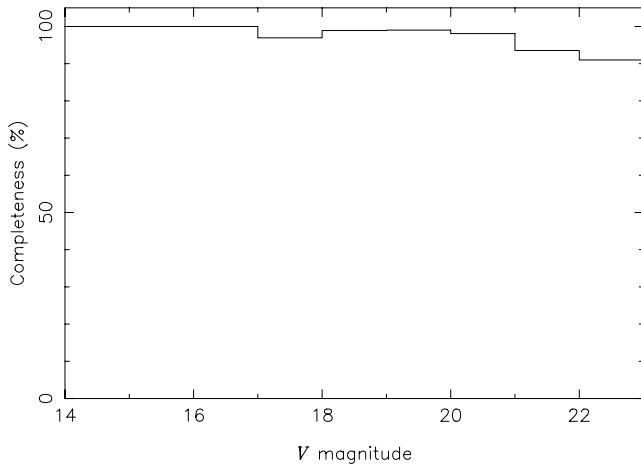


Figure 3. Completeness in our source detection, measured as the fraction of simulated objects which were detected in each magnitude bin. The diagram is plotted in the Johnson V system assuming objects to lie on the empirically derived cluster main-sequence track of Section 3.1 and Fig. 2. The plot has been made only to $V = 23$, corresponding to the termination of the empirical main sequence here.

a simulated catalogue of objects passing our selection criteria at the Galactic coordinates of M34 ($l = 143^\circ 7$, $b = -15^\circ 6$), covering the WFC FOV of $\sim 0.29 \text{ deg}^2$ (including gaps between detectors). We selected all objects over the apparent magnitude range $13 < V < 24$, giving 7625 stars. The same selection process as above for the cluster members was then applied to find the contaminant objects. A total of 283 simulated objects passed these membership selection criteria.

In order to account for the effects of completeness in our source detection, the list of stellar magnitudes from the models was used to

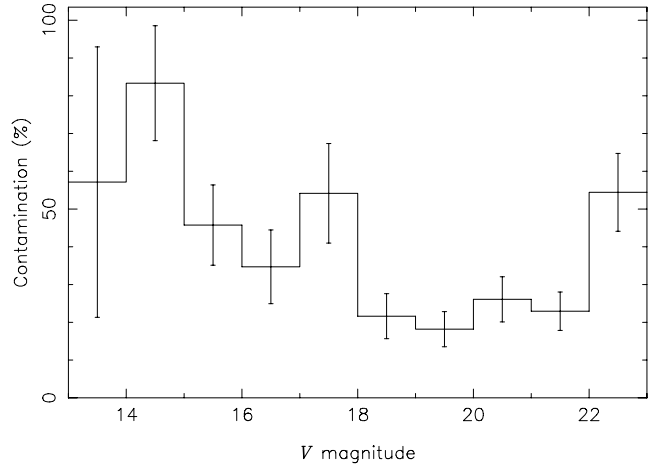


Figure 4. Contamination, measured as the ratio of the calculated number of objects in each magnitude bin from the galactic models, to the number of objects detected and classified as candidate cluster members in that magnitude bin. 1σ Poisson error bars are shown.

insert simulated stars at random x, y positions into our i -band master image. We then ran the source detection software on the resulting simulated image, and kept all the inserted sources that were detected, in order to simulate the detection process, leaving a total of 279 contaminant field stars. This gave an overall contamination level of ~ 39 per cent, and Fig. 4 shows the contamination as a function of V magnitude. We note that this figure is somewhat uncertain due to the need to use galactic models. Follow-up data will be required to make a more accurate estimate.

3.4 Near-IR CMD

In order to check our candidate membership assignments, we used the K -band data for M34 from the Point Source Catalogue of the two-Micron All-Sky Survey (2MASS) to obtain K -band magnitudes for our bright sources (2MASS is complete to $K \sim 14.3$, corresponding to $I \sim 16.5$, $V \sim 18.5$, or $\sim M2$ spectral types in M34). Fig. 5 shows a CMD of K versus $I - K$.

The locations of our photometrically selected candidate cluster members lie along the NextGen isochrone in Fig. 5, indicating that our candidate member selection worked reasonably well over the magnitude range covered by the 2MASS data.

3.5 Alternative methods

We examined alternative methods for membership selection. The use of colour–colour diagrams to reduce contamination was suggested, but found to be of limited use for selection of candidate cluster members, compared to the standard CMD method we used above. The proper motion of M34 is $\sim 20 \text{ mas yr}^{-1}$ (e.g. Jones & Prosser 1996). We examined the possibility of using photographic data sets (in particular the two Palomar Observatory Sky Survey epochs), but the dispersion in the proper motions of $\sim 60 \text{ mas yr}^{-1}$ for the field objects (Jones & Prosser 1996) combined with uncertainties $\sim 10 \text{ mas yr}^{-1}$ at $I > 16$ are too large to allow a clean separation of the cluster from the field for our targets. The only suitable comparison data set for a significant sample of new proper motions is 2MASS, with a $\sim 5 \text{ yr}$ baseline, i.e. total motion of 0.1 arcsec, smaller than the rms astrometric errors. A proper motion study would be feasible in $\sim 15 \text{ yr}$ from the time of writing, when the motion would amount

to ~ 0.4 arcsec (which should be measurable given the ~ 0.1 arcsec rms accuracy of 2MASS). We can nevertheless use proper motions for weeding out rapidly moving foreground objects, and intend to do this for the final membership analysis.

In terms of angular size and density of sources, M34 would be an ideal target for a RV survey using multi-object spectroscopy on 4- or 8-m class telescopes. Obtaining RVs for a large sample of our candidate members could be used to improve the membership selection, using relatively low dispersion, e.g. $R \sim 10\,000$ given the cluster RV of ~ -8 km s $^{-1}$ (estimated from table 3 of Jones & Prosser 1996).

3.6 White dwarfs

A number of faint, blue objects are visible in the CMD of Fig. 2. White dwarfs (WDs) in M34 lie in this region of the diagram, with the WD cooling tracks of Bergeron et al. (private communication) shown as a line on Fig. 2. At such young ages, we may be able to learn about the evolution of young, massive stars from these objects. We have selected seven objects in the CMD lying in the region occupied

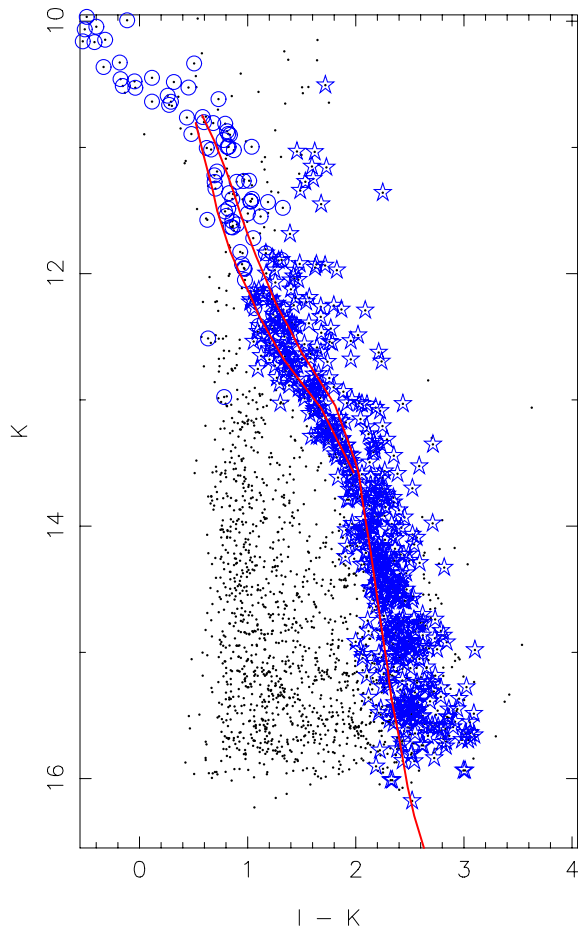


Figure 5. K versus $I - K$ CMD of M34, for all objects with stellar morphological classification. K magnitudes are plotted in the CIT system (Elias et al. 1982, 1983). Objects classified as members in Jones & Prosser (1996) are shown as open circles, and our photometrically selected candidate members are shown as five-pointed stars. The solid lines show the 200-Myr NextGen isochrones of Baraffe et al. (1998) for solar metallicity, with mixing length parameters $L_{\text{mix}} = H_p$ (upper line) and $L_{\text{mix}} = 1.9H_p$ (lower line), where the larger L_{mix} makes a significant difference at high masses ($M \gtrsim 0.6 M_{\odot}$).

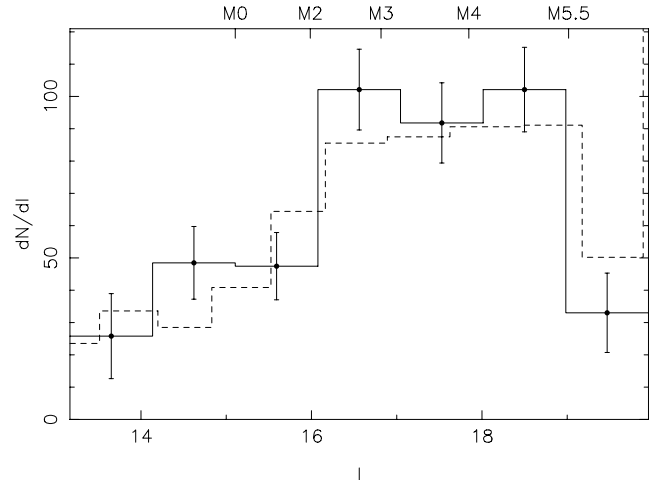


Figure 6. M34 luminosity function (solid line) in apparent I -band magnitude, corrected for contamination. Note that this function has not been corrected for incompleteness in the source detection and cluster membership selection, since the correction is very small over the magnitude range shown. See also Section 3.2 and Fig. 3. The spectral types were determined from the I -band absolute magnitudes for young disc stars of Leggett (1992). The dashed line shows the solar neighbourhood luminosity function of Reid et al. (2002), converted to the I band using our empirical cluster main sequence, and normalized to give the same total number of objects over the I -band magnitude range plotted.

by WDs at the distance of M34 as candidate WD members, to be confirmed spectroscopically.

3.7 Luminosity and mass functions

We have calculated preliminary luminosity and mass functions using the photometric selection. Final versions will be published after we have obtained sufficient additional data to more reliably determine membership for our candidates.

The contamination-corrected luminosity function for M34 is shown in Fig. 6 and tabulated in Table 2, computed from our catalogue of candidate cluster members. Note that the plot range was chosen to correspond to the range over which our sample is close to 100 per cent complete (see Fig. 3). The resulting luminosity function resembles the solar neighbourhood luminosity function of Reid, Gizis & Hawley (2002).

The mass function for M34 has been computed over the range $0.1 \lesssim M/M_{\odot} \lesssim 2.5$ covered by the available data (our sample plus

Table 2. Tabulated contamination-corrected M34 luminosity function (as shown in Fig. 6) in 1-mag bins. I_1 and I_2 denote the start and end of the bin in I , $\langle I \rangle$ the central I value of the bin, and $\sigma(dN/dI)$ gives the estimated uncertainty from Poisson counting errors.

I_1	I_2	$\langle I \rangle$	dN/dI	$\sigma(dN/dI)$
12	13	12.5	3	4
13	14	13.5	18	12
14	15	14.5	41	11
15	16	15.5	49	10
16	17	16.5	101	12
17	18	17.5	92	12
18	19	18.5	101	13
19	20	19.5	33	12
20	21	20.5	-3	3

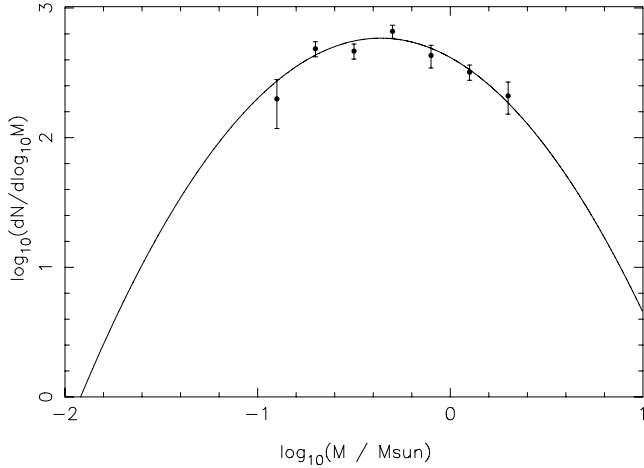


Figure 7. M34 mass function in $dN/d \log M$, corrected for contamination, made using the models of Baraffe et al. (1998) to calculate a mass for each object from the I magnitude. The solid line shows a lognormal fit to dN/dM , i.e. a quadratic fit to $\log(dN/d \log M)$, with parameters $M_0 = 0.44 M_\odot$ (the mass at maximum dN/dM), and $\sigma = 0.66$. We have used the catalogue of M34 proper motion members from Jones & Prosser (1996) to populate the two highest-mass bins. Note that the projected areas covered by these surveys are similar, but the centres are offset by a few arcmin, so the actual coverage of M34 members may differ, which will affect the results for the upper two bins.

proper motion members of M34 from Jones & Prosser 1996) with close to 100 per cent completeness. The lower limit results from the drop in completeness at $I \simeq 20$ for our sample, and the upper limit from the upper mass limit of the models of Baraffe et al. (1998). The result is shown in Fig. 7 and tabulated in Table 3. In order to produce these distributions, the observed number counts from our survey were corrected for field star contamination using the Besançon model star counts of Section 3.3. For the data from Jones & Prosser (1996), we chose only those objects with membership probabilities $P > 80$ per cent. The masses were computed from the I -band magnitudes using the models of Baraffe et al. (1998), using a linear extrapolation from the high-mass end for the brightest objects from Jones & Prosser (1996).

We find that a lognormal mass distribution of the form

$$\frac{dN}{d \log M} \propto \exp \left[-\frac{\log M - \log M_0}{2\sigma^2} \right] \quad (4)$$

is a good fit to the data in $dN/d \log M$. Parametrized by a mass at maximum $dN/d \log M$ of $M_0 = 0.44 \pm 0.31 M_\odot$ and $\sigma = 0.66 \pm 0.08$. These are in relatively good agreement with the values of $M_0 \sim 0.3 M_\odot$ and $\sigma \sim 0.5$ derived by Moraux, Bouvier & Clarke

Table 3. Tabulated M34 mass function in $dN/d \log M$. M_1 and M_2 denote the start and end of the bin in M , $\langle \log_{10} M \rangle$ the central $\log_{10} M$ value of the bin, and $\sigma(dN/d \log M)$ gives the estimated uncertainty from Poisson counting errors.

$\log_{10} M_1$	$\log_{10} M_2$	$\langle \log_{10} M \rangle$	$dN/d \log M$	$\sigma(dN/d \log M)$
-1.0	-0.8	-0.9	642	263
-0.8	-0.6	-0.7	1046	139
-0.6	-0.4	-0.5	633	84
-0.4	-0.2	-0.3	567	65
-0.2	0.0	-0.1	233	46
0.0	0.2	0.1	109	15
0.2	0.4	0.3	54	15

(2005) for a sample of three young open clusters. It should be noted that our survey covered only the central part of the cluster,⁴ and it is likely that the low-mass members are distributed with a larger core radius than the higher-mass members, implying a bias toward higher masses. Unfortunately, our present survey does not have sufficient sky coverage to resolve this problem. It should also be noted that these conclusions were made on the basis of measurements over a very small range in mass. More data at higher or lower masses would improve the situation and allow us to examine the mass function in greater detail.

4 PERIOD DETECTION

4.1 Method

The limited time baseline of only 10 nights for our observations is insufficient to make a detailed study of stellar rotation periods $\gtrsim 10$ d. However, our observations have relatively good sensitivity to short-period (e.g. $\lesssim 10$ d) systems so a careful examination of the data for rotation and other periodic variability has been carried out.

Variable objects were selected using least-squares fitting of sine curves to the time-series $m(t)$ (in magnitudes) for all sources in the CCD images, using the form

$$m(t) = m_{dc} + \alpha \sin(\omega t + \phi), \quad (5)$$

where m_{dc} (the DC light-curve level), α (the amplitude) and ϕ (the phase) were free parameters at each value of ω over an equally spaced grid of frequencies, corresponding to periods from 0.005–20 d. The lower period limit was chosen to correspond to the cadence of our observations, and the upper limit to the observing window, estimating that we still have a chance of recovering the correct period after observing only half a cycle (see also Section 4.2). The output of this procedure is a ‘least-squares periodogram’, with the best-fitting period being the one giving the smallest reduced χ^2 .

All of the light curves were processed in this manner. In order to distinguish the variable objects from the non-variable objects, we used the reduced χ^2 , but evaluated by subtracting a smoothed, phase-folded version of each light curve at the best-fitting period. The smoothing was carried out using median filtering over a 51 data point window, followed by a linear boxcar filter over an 11 data point window to smooth out any high-frequency features. This procedure accounts for any non-sinusoidal (but otherwise periodic) features in the light curve, and we have found empirically that it is capable of detecting somewhat non-sinusoidal variables such as detached eclipsing binaries and even the transiting extrasolar planet OGLE-TR-56b (Konacki et al. 2003) from the published light-curve data.

Periodic variable light curves were selected by evaluating the change in reduced χ^2 :

$$\Delta \chi_v^2 = \chi_v^2 - \chi_{v,smooth}^2 > 0.4, \quad (6)$$

where χ_v^2 is the reduced χ^2 of the original light curve with respect to a constant model, and $\chi_{v,smooth}^2$ is the reduced χ^2 of the light curve with the smoothed, phase-folded version subtracted. We used a simple cut in $\Delta \chi_v^2$ rather than $\Delta \chi_v^2 / \sigma(\chi^2)$ (where $\sigma(\chi^2)$ is the rms of the χ^2 measure, depending only on the number of data points) because our error estimates are somewhat unreliable, and therefore $\sigma(\chi^2)$

⁴ At a distance of 470 pc, 1 pc ~ 0.12 , and our survey covers a radius of ~ 0.2 , similar to typical cluster core radii of a few pc.

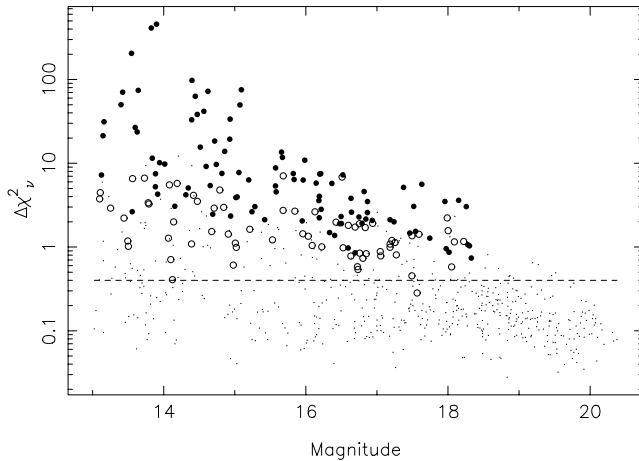


Figure 8. $\Delta\chi_v^2$ as a function of i -band magnitude for candidate M34 cluster members. The horizontal line shows the threshold at $\Delta\chi_v^2 > 0.4$, with solid circles indicating objects with clear periodic variability, open circles indicating the ambiguous cases, and small points indicating objects without periodic variability (non-variable light curves or those showing irregular variability).

underestimates the true dispersion of the χ_v^2 value for a featureless light curve.

The threshold of $\Delta\chi_v^2 > 0.4$ was chosen as follows. All of the 714 light curves of candidate cluster members were examined by eye, looking for variability, and placing the objects into four bins: objects with clear periodic variability, objects with clear non-periodic variability, ambiguous cases and non-variable light curves. The numbers of objects falling in each bin were 102, 8, 67 and 537, respectively. Fig. 8 shows these objects on a diagram of $\Delta\chi_v^2$ as a function of magnitude.

The threshold was chosen to select at least all of the clear periodic variables and the more significant of the ambiguous light curves. Applying the threshold gave 283 detections, after also removing objects lying on bad pixels for more than 10 per cent of their light-curve points, non-stellar objects (by morphological classification) and any object with data points spanning a range of less than 1/2 of the orbital phase. Note that objects flagged as blended were not removed since a large fraction of these were sufficiently uncontaminated to still be used. Only three of the light curves classified as ambiguous were rejected, and these were visually confirmed to be poor detections that were not obviously variable.

After applying the threshold, the selected light curves were examined independently by eye, to select the final sample included here. A total of 105 light curves were selected, with the remainder appearing non-variable or too ambiguous to be included.

Our periods derived from the selection procedure described were refined by using both the V - and i -band light curves simultaneously, fitting a separate set of coefficients m_{dc} , α and ϕ in each band, but combining the χ^2 values to produce a periodogram taking both bands into account. We have not used this method for the detection process itself because it is difficult to simulate for evaluating completeness, necessitating assuming a relation between the V - and i -band amplitudes and magnitudes for the simulated objects. Furthermore, at the faint end, where the detection begins to become incomplete, the signal to noise in the V band is very poor for cluster members, so using the V band does not give any improvement.

4.2 Simulations

The large amount of human involvement in our selection procedure is difficult to simulate in an unbiased manner. Nevertheless, we have attempted to evaluate our selection biases by performing Monte Carlo simulations, injecting sinusoidal modulations into non-variable M34 light curves, selected by requiring $\chi_v^2 < \langle \chi_v^2 \rangle + 3\sigma(\chi_v^2)$ (calculated using robust MAD – median of absolute deviations from the median – estimators in 0.5 mag bins) to remove the most variable objects. These were then subjected to exactly the same selection procedure as the real light curves, detailed in Section 4.1, including examination by eye.

In order to reduce biases in the detection process resulting from ‘knowing’ that the modulations are real, modulations were not inserted into a fraction (1/6) of the light curves shown to the human. A larger fraction (1/2) would be more realistic but would increase the already rather large number of light curves that must be examined.

Each simulation was run following uniform distributions in \log_{10} period from 0.1 to 20 d, and a uniform distribution in mass from 1.0 to 0.1 M_{\odot} , the second satisfied by choosing light curves in the correct magnitude range for each 0.1 M_{\odot} bin. Phases ϕ were chosen at random in $0 \leq \phi < 2\pi$, and the exercise was repeated for three typical amplitudes, 0.01, 0.02 and 0.05 mag, corresponding approximately to the range of values for M34 rotators that we detected. ~ 2000 periodic variable objects were simulated in each amplitude bin.

The results of the simulations are shown in Fig. 9 as grey-scale diagrams of completeness, reliability and contamination as a function of period and stellar mass. Broadly, our period detections are close to 100 per cent complete for $P < 10$ d and $M \gtrsim 0.4 M_{\odot}$.

As with all ground-based observations, our period determinations suffer problems of aliasing. The most serious of these is at a frequency spacing of 1 d^{-1} corresponding to the observing gaps during the day, and leads to periodogram peaks at the ‘beat’ periods

$$\frac{1}{P_{\text{beat}}} = \frac{1}{P} \pm 1, \quad (7)$$

where P is the true period. Fig. 10 illustrates this effect using our simulated light curves. Using both V and i bands to refine the period estimates mitigates the effect slightly (since the observations were not precisely simultaneous), but this has not been accounted for in the simulations.

4.3 Detection rate and reliability

The locations of our detected periodic variable candidate cluster members on a V versus $V - I$ CMD of M34 are shown in Fig. 11. The diagram indicates that the majority of the detections lie on the single-star cluster main sequence, as would be expected for rotation in cluster stars as opposed to, say, eclipsing binaries.

Fig. 12 shows the fraction of cluster members with detected periods as a function of i magnitude. The rise from the bright end towards lower masses indicates that M dwarfs may show more spot-related rotational variability within our detection limits than K or G dwarfs. This would be consistent with an increase in spot coverage moving to later spectral types. The decaying portion of the histogram from $i \sim 15$ is likely to be an incompleteness effect resulting from the gradual increase in the minimum amplitude of variations we can detect (corresponding to the reduction in sensitivity moving to fainter stars, see Fig. 1) and not a real decline.

The phase-folded light curves of all our rotation candidates are shown in Fig. A1, and their properties summarized in Table A1 (see Appendix A).

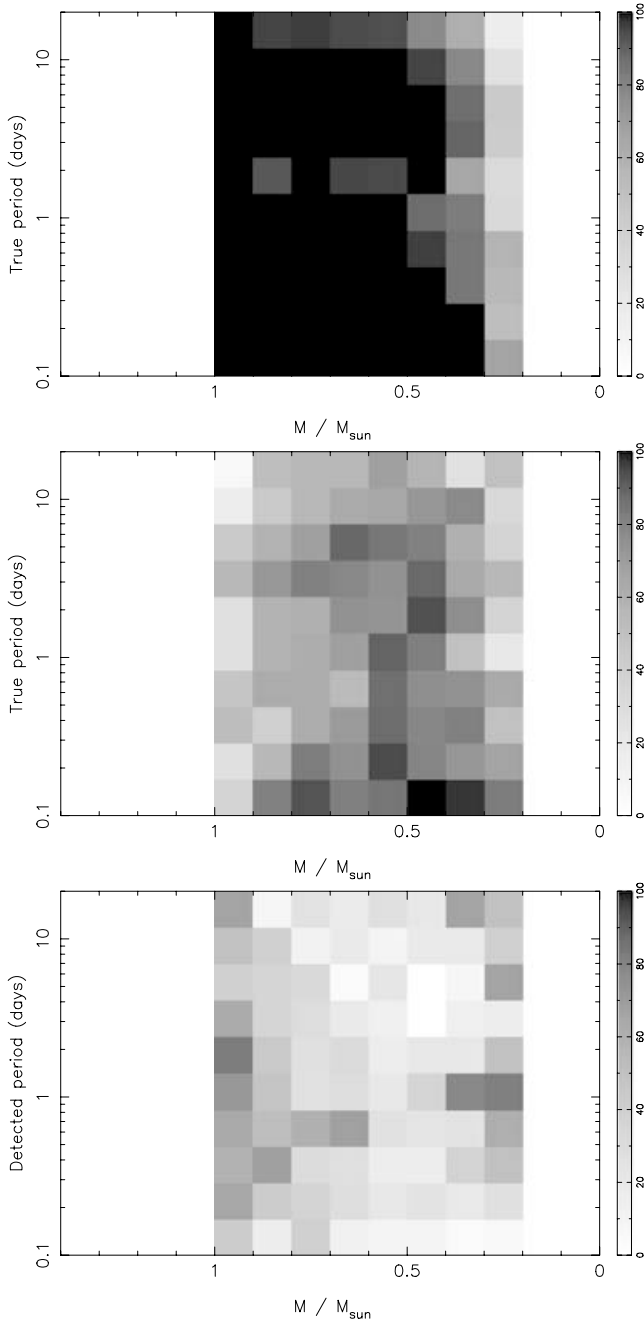


Figure 9. Results of the simulations for 0.02 mag amplitude as grey-scale maps, where black corresponds to 100 per cent and white to 0 per cent. The simulated region covered $0.2 < M/M_{\odot} < 1.0$ in order to be consistent with the M34 sample. Top panel: completeness as a function of real (input) period. Centre panel: reliability of period determination, plotted as the fraction of objects with a given true period, detected with the correct period (defined as differing by < 20 per cent from the true period). Bottom panel: contamination, plotted as the fraction of objects with a given detected period, having a true period differing by > 20 per cent from the detected value.

4.4 Non-periodic objects

The population of objects rejected by the period detection procedure described in Section 4 was examined, finding that the most variable population of these light curves (which might correspond to non-periodic or semiperiodic variability) was contaminated by

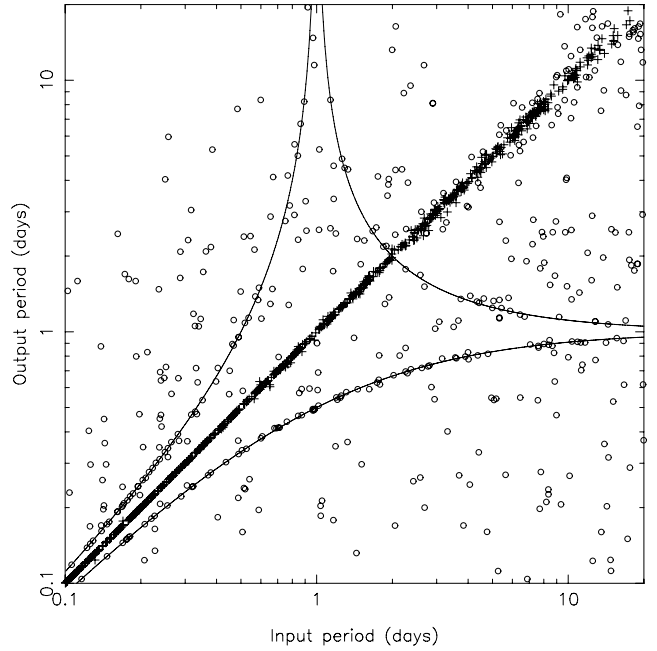


Figure 10. Detected period as a function of actual (input) period for our simulations. Objects plotted with crosses had fractional period error < 10 per cent, open circles > 10 per cent. The straight line represents equal input and output periods. The curved lines are the loci of the $\pm 1 \text{ d}^{-1}$ aliases from equation (7). The majority of the points fall either on (or close to) the line of equal periods, or on one of the curves consistent with 1 d^{-1} aliasing.

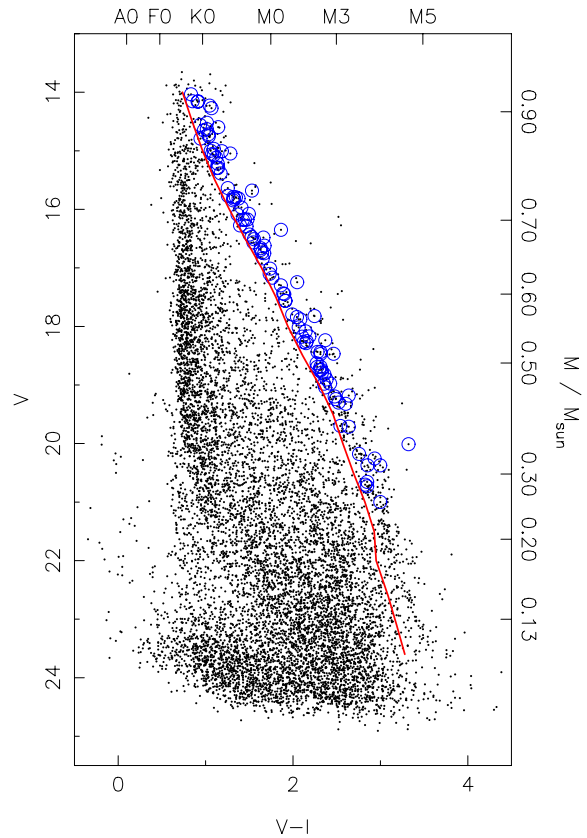


Figure 11. V versus $V-I$ CMD of M34, for all objects with stellar morphological classification, as Fig. 2, showing all 105 candidate cluster members with detected periods (open circles).

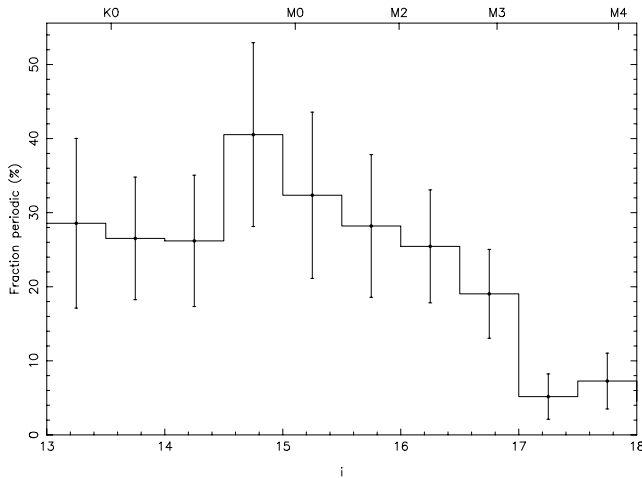


Figure 12. Fraction of candidate cluster members detected as periodic variables, plotted as a function of magnitude. This distribution has not been corrected for incompleteness in the period detections, so the decaying portion of the histogram from $i \sim 15$ is likely to be an incompleteness effect resulting from the gradual increase in the minimum amplitude of variations we can detect, as a function of increasing magnitude (and hence increasing noise, see Fig. 1), and not a real decline.

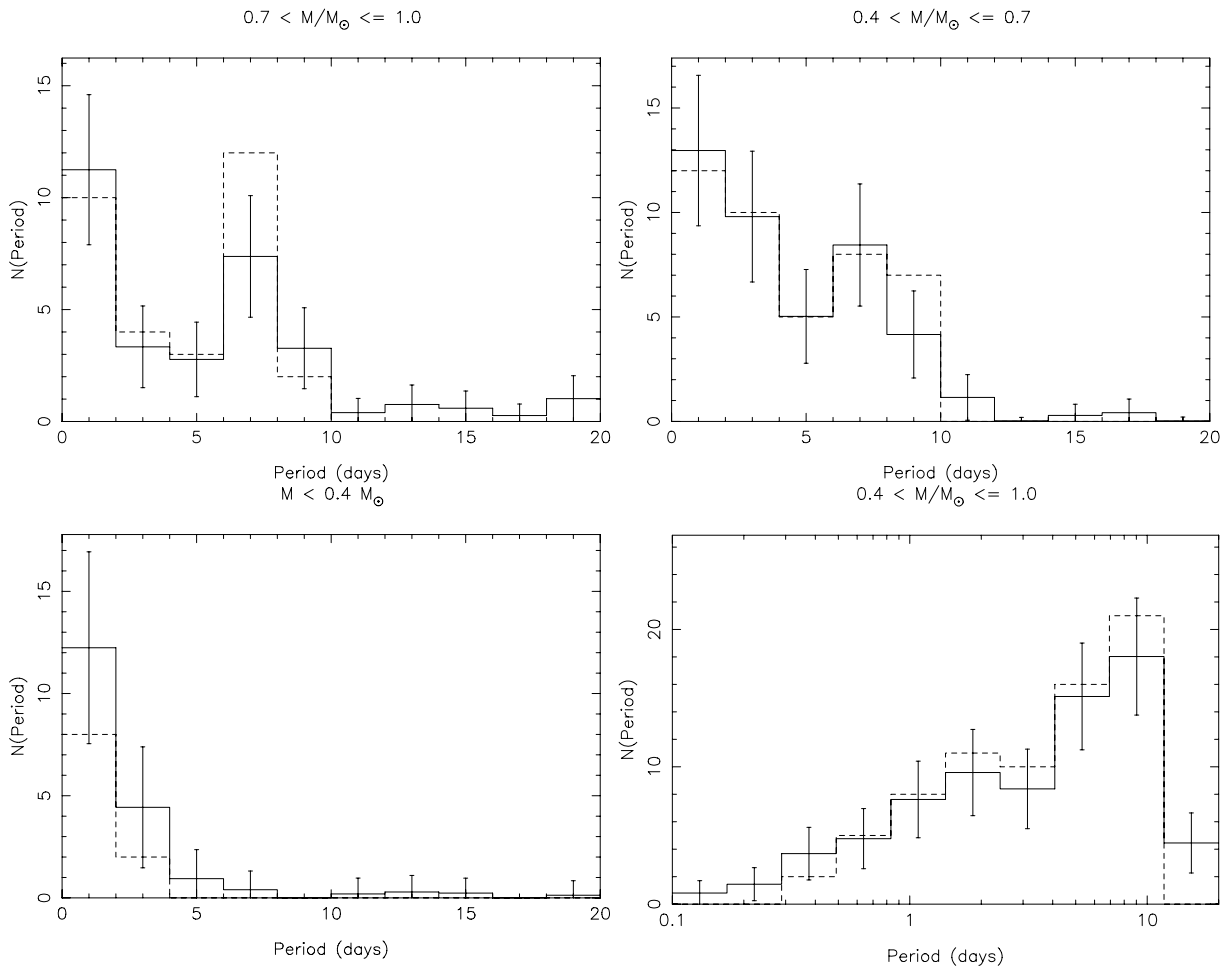


Figure 13. Period distributions for objects classified as possible photometric members, in three mass bins: $0.7 \leq M/M_{\odot} < 1.0$ (corresponding roughly to late-G and K spectral types), $0.4 \leq M/M_{\odot} < 0.7$ (early-M) and $M < 0.4 M_{\odot}$ (late-M and VLM). The bottom right-hand panel shows the period distribution for $0.4 \leq M/M_{\odot} < 1.0$ plotted in \log_{10} period, indicating that the apparent bimodality in this mass range is probably not significant. The dashed lines show the measured period distributions, and the solid lines show the results of attempting to correct for incompleteness and reliability, as described in the text. Objects with periods flagged as unreliable in Table A1 have been excluded.

a number of light curves exhibiting various uncorrected systematic effects. It is therefore difficult to quantify the level of non-periodic or semiperiodic variability in M34 from our data. Qualitatively however, there appear to be very few of these variables, and examining the light curves indicated only ~ 3 obvious cases, which strongly resembled eclipses (either planetary transits or eclipsing binaries), and will be the subject of a later Monitor project paper.

5 RESULTS

5.1 Periods and rotational velocities

Period distributions for the objects photometrically selected as possible cluster members are shown in Fig. 13, a plot of period as a function of $V - I$ colour is shown in Fig. 14, and plots of period and amplitude as a function of mass are shown in Figs 15 and 16, respectively.

5.1.1 Period distributions

We have attempted to correct the period distribution for cluster members in Fig. 13 for the effects of incompleteness and (un)reliability using the simulations described in Section 4.2. The results are shown in the solid histograms in Fig. 13. This histogram was generated as

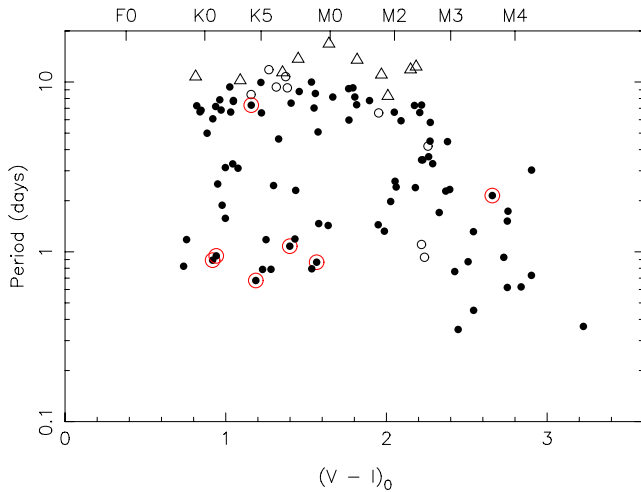


Figure 14. Plot of rotation period as a function of dereddened $V - I$ colour for M34. X-ray sources from Simon (2000) are overlaid with open circles. Open symbols indicate objects flagged ‘a’ (open circles) and ‘b’ (open triangles) in Table A1.

follows: for each bin of the period distribution as a function of *detected* period, containing N_i objects, we chose N_i random objects falling in that bin from the simulations, and generated a new histogram using the *real* periods of the simulated objects. We then averaged over 1000 realizations of this process. This has the effect of converting the histogram plotted as a function of *detected* period to one plotted as a function of *real* period. This was then corrected for incompleteness by dividing by the completeness fraction from Fig. 9.

We applied two-sided Kolmogorov–Smirnov (KS) tests to the corrected distributions in adjacent mass bins to evaluate whether the visible differences between the distributions were statistically significant. In particular, there is an apparent clear distinction between the distribution for $M > 0.4 M_{\odot}$ and $M < 0.4 M_{\odot}$, in the sense that there are few slow rotators at low mass. The results are summarized in Table 4.

The KS test for the first two mass bins is inconsistent with there being significant differences in the period distribution. However, the test for the $0.4 \leq M/M_{\odot} < 0.7$ and $M < 0.4 M_{\odot}$ bins indicates that they differ significantly at the 99.8 per cent confidence level, i.e. the VLM stars ($M < 0.4 M_{\odot}$) show a different period distribution than the higher-mass stars ($M > 0.4 M_{\odot}$). This effect is also visible in Fig. 15, and is discussed further in Section 5.1.5.

5.1.2 Bimodality?

The period distributions for $M > 0.4 M_{\odot}$ in Fig. 13 appear to be bimodal when plotted in linear period (see also Fig. 15), but the apparent bimodality is much less obvious in \log_{10} period (see the lower right-hand panel of Fig. 13). Following Stassun et al. (1999), we attempted to determine whether this bimodality is statistically significant by performing a one-sample KS test against a model distribution, taken to be a simple function $N(P) = 30(1 - P/15)$, fit by eye to the upper envelope of the distribution, over $0 < P < 15$ d. The result was a 28 per cent probability that our period distribution was indeed drawn from this simple model distribution. The high probability for this poor model coupled with the results in \log_{10} period implies that the apparent bimodality is not significant.

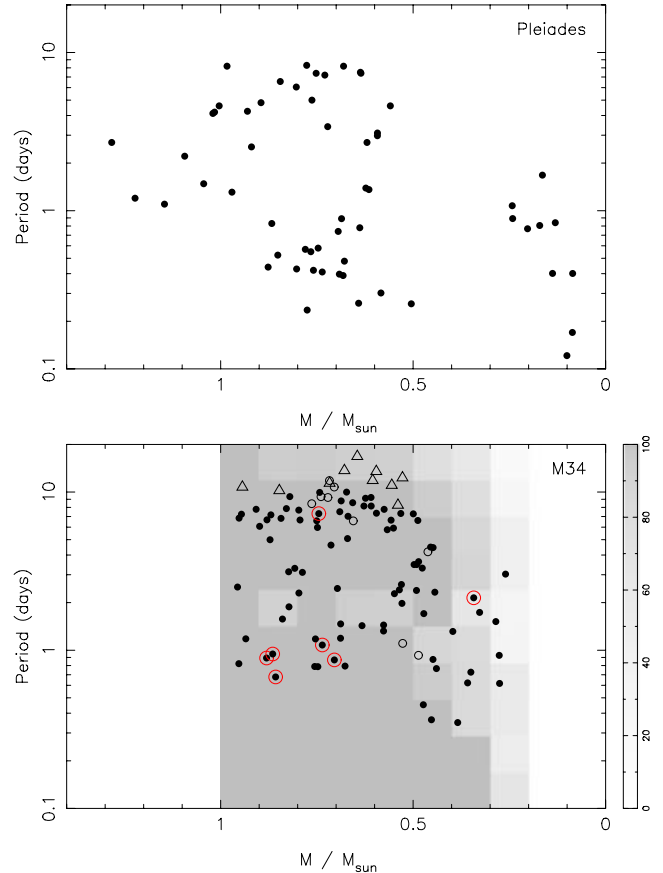


Figure 15. Plot of rotation period as a function of mass for the Pleiades (top) and M34 (bottom). Ages: 125 Myr (Stauffer et al. 1998) and 200 Myr. Masses were interpolated from the model isochrones of Baraffe et al. (1998) using the I -band magnitudes (two Pleiades objects without this information were excluded). The Pleiades data are a compilation of the results from Van Leeuwen, Alphenaar & Meys (1987), Stauffer et al. (1987), Magnitskii (1987), Prosser et al. (1993a,b, 1995), Krishnamurthi et al. (1998) (taken from the open cluster data base), Terndrup et al. (1999) and Scholz & Eislöffel (2004). Symbols for M34 as Fig. 14, with the grey-scales showing the completeness for 0.02 mag periodic variations from Fig. 9.

Truly bimodal distributions are typically seen only in much younger clusters (e.g. the ONC; Herbst et al. 2002), although there is evidence that this may also be the case in the Pleiades (e.g. Soderblom et al. 1993a) and are generally interpreted as resulting from the presence of a mixture of disc-locked and unlocked, spun-up stars (see Section 1.1). Such an interpretation cannot hold at the age of M34.

Interestingly, the presence of a short-period peak at $P \sim 1\text{--}2$ d and a longer period peak at $P \sim 7$ d is consistent with the empirical view on angular momentum evolution of Barnes (2003). Briefly, the short-period peak corresponds to the C or ‘convective’ sequence, and the long-period peak to the I or ‘interface’ sequence. In this interpretation, stars on the C sequence have decoupled radiative and convective zones, with angular momentum loss due to stellar winds coupled to convective magnetic fields. On the I sequence, an interface dynamo couples the zones leading to increased angular momentum loss (Barnes 2003). Very low-mass stars (e.g. $M < 0.4 M_{\odot}$ in Fig. 13) are fully convective, so they can only lie on the C sequence and hence fall at short periods.

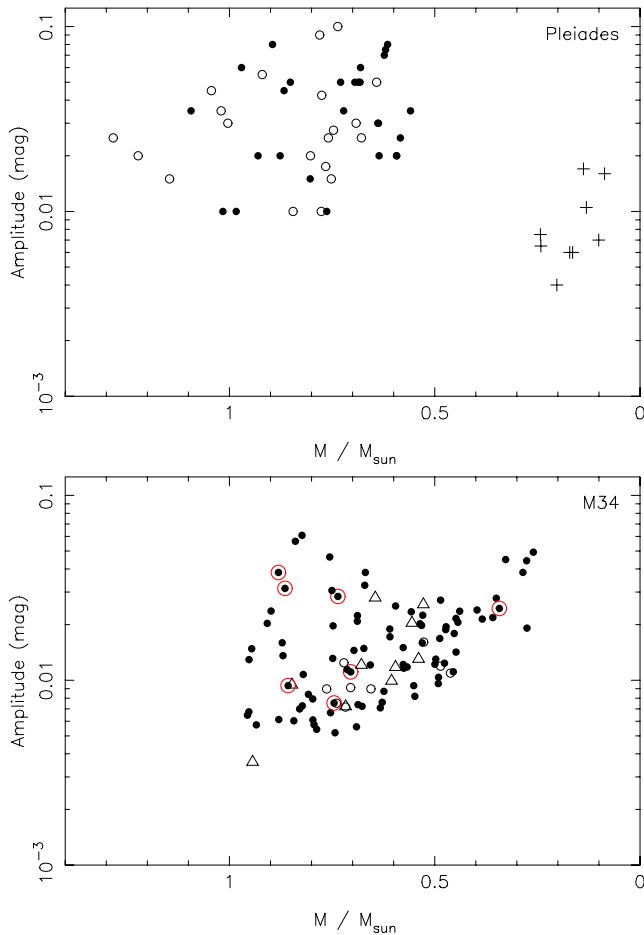


Figure 16. Plot of amplitude as a function of mass for the Pleiades (top) and M34 (bottom). The Pleiades amplitudes have been converted to the semi-amplitude as used in this work, and the passband used is indicated by the symbols: filled circles indicate V band, crosses indicate I band, and open circles denote objects with amplitudes measured in unknown passbands (but suspected to be V). All symbols in the M34 plot are as Fig. 15 with all objects measured in i band. The lower envelope of this diagram clearly traces the rms curve in Fig. 1 and therefore results from incompleteness at low amplitude for faint stars resulting from increased noise.

Table 4. Results of two-sided KS tests to evaluate the probabilities that the period distributions in adjacent mass bins are drawn from the same parent population.

Mass range 1	Mass range 2	P (same)
$0.7 \leq M/M_{\odot} < 1.0$	$0.4 \leq M/M_{\odot} < 0.7$	0.85
$0.4 \leq M/M_{\odot} < 0.7$	$M < 0.4 M_{\odot}$	2×10^{-3}

5.1.3 Rapid rotators

The presence of rapid rotation (e.g. $P < 1$ d) at the age of M34 is important for constraining models of angular momentum evolution, discussed in Section 5.2. We have examined the periods of these stars, to check that they are not rotating close to their break-up velocity, where they would be short-lived, suggestive of spin-up on the ZAMS. The corresponding critical period P_{crit} for break-up is given approximately by

$$P_{\text{crit}} = 0.116 \text{ d} \frac{(R/R_{\odot})^{3/2}}{(M/M_{\odot})^{1/2}}, \quad (8)$$

where R and M are the stellar radius and mass, respectively (e.g. Herbst et al. 2002). Using the models of Baraffe et al. (1998), the object rotating closest to its critical period is M34-1-2402, at $P = 0.260$ d, where $P_{\text{crit}} = 0.039$ d, a factor of 7 shorter, so we find no objects in M34 rotating close to break-up.

5.1.4 0.4 – $1.0 M_{\odot}$ objects

Comparing the distributions of rotational periods for M34 and the Pleiades in Fig. 15 indicates that, in general, the M34 distribution resembles a ‘spun-down’ Pleiades distribution, exactly as expected. However, several conspicuous objects are visible in Fig. 15, with periods close to 1 d and high masses (~ 0.8 – $1.0 M_{\odot}$). These are somewhat difficult to explain by spin-down of faster Pleiades rotators, given the lack of < 1 d period rotators there for $M \gtrsim 0.9 M_{\odot}$ (see Fig. 15), but the discrepancy could result from $\sim 0.1 M_{\odot}$ errors in the computation of the masses, dominated by errors in determining the I magnitudes (in particular for the Pleiades data, due to the conversions required between the photometric systems used by the various authors).

The light curves for these objects were examined carefully, finding two very significant detections at unusually large amplitude with associated X-ray sources, M34-1-2953 and M34-3-523. Detection in X-rays is suggestive of youth or binarity. Since these objects are at high-mass and hence subject to increased field contamination, it is possible that they may be field objects. One further object was detected in X-rays, M34-4-1092, with a ~ 1 per cent amplitude, and interestingly is the only one of these objects lying away from the cluster sequence, being ~ 0.5 mag brighter. We therefore suspect that it is a binary, to be confirmed spectroscopically. The remaining objects, M34-4-2697 and M34-4-2833, are two of our lowest-amplitude rotation candidates (~ 0.5 per cent) and are marginal detections. Our planned spectroscopy of all the candidates should allow us to weed out any field contaminants, and to measure $v \sin i$ for any very rapid rotators to confirm their nature.

On the suggestion of the anonymous referee, we note the strong resemblance between the M34 results in Fig. 15 and the Pleiades $v \sin i$ distribution of Soderblom et al. (1993a). These authors also found the majority (80 per cent) of the rotators to have low velocities, with an upper branch of rapid rotators comprising the remainder of the sample.

Accounting for the differences in sensitivity between the surveys, Fig. 16 shows no significant evolution in amplitude from the Pleiades to M34. However, we do find an apparent trend of decreasing amplitude moving to lower masses, down to $\sim 0.4 M_{\odot}$ in M34. It is not clear whether a similar trend exists in the Pleiades over this mass range due to the lack of data.

5.1.5 $< 0.4 M_{\odot}$ objects

Fig. 13 shows a clear and statistically significant lack of slow rotators in the period distribution for $M < 0.4 M_{\odot}$. This appears to be a real effect, and is not caused, for example, by selection biases in our sample. This effect has been observed previously (e.g. Scholz & Eislöffel 2004) at very low mass, but we were unable to find significant samples of rotation periods in the literature for the mass range $0.25 < M/M_{\odot} < 0.4$ probed by our sample, so it is complementary to these previous studies.

Tentatively the data in this mass range suggest that the typical rotation periods of these stars decrease as a function of decreasing mass, i.e. less massive stars are faster rotators. This is in good agreement

with the results at very low mass ($M \lesssim 0.25 M_{\odot}$) from Scholz & Eislöffel (2004), who found the rather slow spin-down of VLM stars to be better fit by models assuming an exponential angular momentum loss law, giving $P \propto e^t$, rather than the Skumanich (1972) $t^{1/2}$ law that applies for higher-mass stars. They attribute this difference to the fully convective nature of the low-mass objects, which cannot support a large-scale magnetic dynamo, which gives rise to the Skumanich (1972) angular momentum loss law in solar mass stars. We cannot make a detailed assessment of these conclusions over the mass range $0.25 < M/M_{\odot} < 0.4$, since we could not find a suitable equivalent large sample of stars with measured rotation periods in a young open cluster from the literature. This will be addressed by the Monitor project, where we have obtained photometric periods for low-mass stars in several young clusters, including NGC 2516 (~ 150 Myr; Jeffries, Thurston & Hambly 2001), M50 (~ 130 Myr; Kalirai et al. 2003) and NGC 2362 (~ 5 Myr; Moitinho et al. 2001), to be presented in a future publication.

Scholz & Eislöffel (2004) found significantly lower amplitudes for $M < 0.25 M_{\odot}$ than for the higher-mass ($M \gtrsim 0.5 M_{\odot}$) Pleiades objects (see Fig. 16). We see no evidence for this in the interval $0.25 < M/M_{\odot} < 0.4$, finding instead amplitudes comparable to those of the stars in the higher-mass bin. We cannot test the result in M34 for $M < 0.25 M_{\odot}$ with the present data set.

5.1.6 Comparison with $v \sin i$ measurements

We have compared our sample of objects with the spectroscopic sample of Soderblom et al. (2001). Due to the different magnitude ranges, we only have 22 objects in common, and obtained photometric periods for 12 of these. The 10 objects missed did not show significant periodic variability during visual examination of the light curves. Fig. 17 shows a comparison of the $v \sin i$ values with v_{rot} derived from our photometric periods, derived as

$$v_{\text{rot}} = \frac{2\pi R}{P}, \quad (9)$$

with stellar radii R taken from the models of Baraffe et al. (1998).

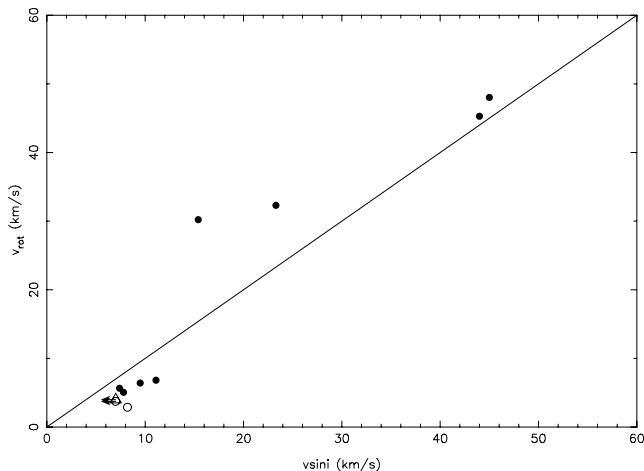


Figure 17. Plot of the photometric rotation velocity v_{rot} as a function of the $v \sin i$ value measured by Soderblom et al. (2001). The diagonal line indicates the case where $v \sin i = v_{\text{rot}}$, and the region above the line corresponds to the ‘allowed’ region where $v \sin i < v_{\text{rot}}$. The small population of objects with $v \sin i$ slightly greater than v_{rot} may result from overestimation of the $v \sin i$ values and are close to the lower measurable limit for the spectroscopic observations of Soderblom et al. (2001). Alternatively, these could highlight deficiencies in the model radii we have used to derive v_{rot} .

We note that the long-period end of all the figures presented in this section is somewhat affected by the short observing window we had available, and should therefore be treated with caution. Nevertheless, we believe that useful conclusions can still be drawn from the data.

5.2 Rotational evolution

The ranges of measured rotation periods in IC 2391, IC 2602, α Per, the Pleiades, M34 and the Hyades are compared in Fig. 18. The samples for IC 2391 and IC 2602 have been combined due to the very similar distance moduli and ages of these clusters. We use the lower and upper 10 percentile of the rotational period distributions to trace the evolution of the rapid and slow rotators, respectively. The convergence in rotation rates across the full age range from IC 2391 and IC 2602 at ~ 30 Myr to the Hyades (~ 625 Myr; Perryman et al. 1998) is clearly visible in the diagram, due to spin-down of the rapid rotators by a greater amount than the slow rotators. The diagram also indicates the differences in evolution between (roughly) K and M stars, although it is difficult to constrain the latter because the samples we have gathered from the literature in α Per and the Hyades are substantially incomplete at low masses.

We caution that the samples in Fig. 18 were taken from a wide variety of sources and may not be directly comparable. The reliability of the long periods in our M34 sample may be reduced by our limited time baseline. For the rapid rotators, the 10 percentile may be affected by field contamination (due to field objects misclassified as cluster members), for example contact binary systems, which have very short photometric periods, but are otherwise difficult to distinguish from rotational modulation at low amplitude.

The rotational evolution can be simply modelled by assuming that it results from two components: the spin-up due to contraction in stellar radius (while conserving total angular momentum) as a function of age, which we compute from the models of Baraffe et al. (1998), and spin-down resulting from angular momentum loss:

$$P_2 = \alpha P_1 \left(\frac{R_2}{R_1} \right)^2, \quad (10)$$

where P_1 and P_2 are the rotation periods at the two ages, R_1 and R_2 are the corresponding stellar radii, and α is a multiplicative factor resulting from angular momentum loss.

The simple Skumanich (1972) law gives

$$\alpha_{\text{sk}} = \left(\frac{t_2}{t_1} \right)^{1/2}, \quad (11)$$

where t_1 and t_2 are the respective ages ($t_1 < t_2$). The predictions of this model are compared with the observations in Fig. 18. The results indicate that in general, the angular momentum loss law (11) loses angular momentum too slowly between the Pleiades and M34, and likewise for the fast rotators between M34 and the Hyades. It appears to lose angular momentum (slightly) too quickly for the slow rotators from M34 to the Hyades, although the latter conclusion depends on our measured slow rotation periods, which may be unreliable. We suggest that the observations require a more rapid spin-down from the Pleiades to M34, followed by flattening between M34 and the Hyades.

Our results do however appear to be consistent with more comprehensive models of angular momentum evolution assuming solid body rotation, for example Bouvier et al. (1997), where the maximum rotational velocity decreases from $v_{\text{max}} = 100 \text{ km s}^{-1}$ ($P \sim 0.5 \text{ d}$ at M_{\odot}, R_{\odot}) at the age of the Pleiades to $v_{\text{max}} = 50 \text{ km s}^{-1}$ ($P \sim 1 \text{ d}$) at the age of M34, roughly as observed. Models incorporating core–envelope decoupling (e.g. Allain 1998, see also fig. 3 of

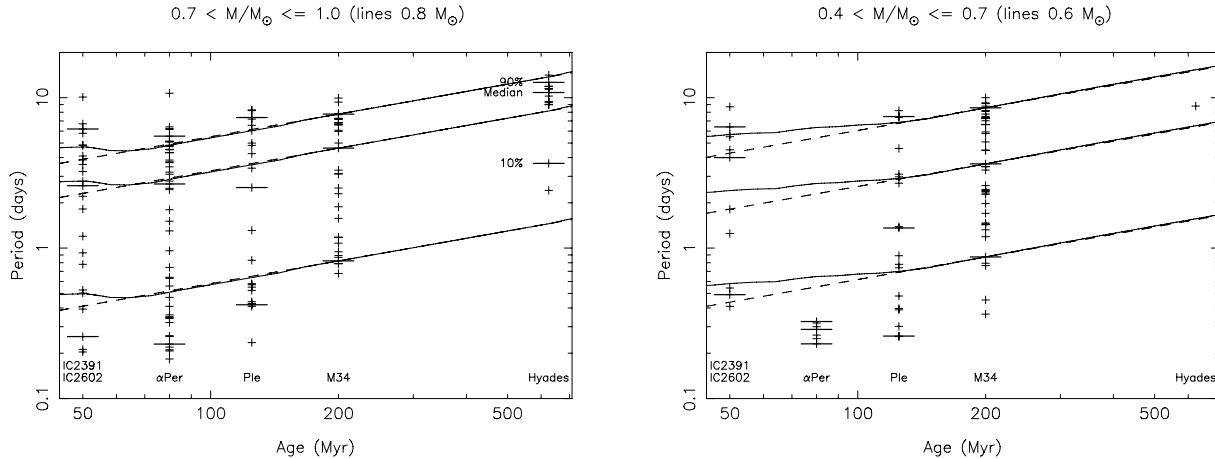


Figure 18. Plot of the IC 2391, IC 2602 (~ 50 Myr; Barrado y Navascués, Stauffer & Jayawardhana 2004), α Per (~ 80 Myr; Stauffer et al. 1999), Pleiades, M34 (using all of our period detections to avoid biasing the distribution against long periods) and Hyades rotation periods as a function of time, in two mass bins: $0.7 \leq M/M_{\odot} < 1.0$ (corresponding roughly to G and K spectral types) and $0.4 \leq M/M_{\odot} < 0.7$ (early-M). A similar diagram was not plotted for the $M < 0.4 M_{\odot}$ (late-M and VLM) bin of Fig. 13 since there were no suitable samples in the other clusters covering the same mass range ($0.25 < M/M_{\odot} < 0.4$). The upper and lower 10 percentile of the period distributions, and their medians, are shown as short horizontal lines. The change in the median indicates the convergence toward long periods moving from the Pleiades, to M34, to the Hyades. The IC 2391 data were taken from Patten & Simon (1996) and IC 2602 from Barnes et al. (1999). The α Per data are a compilation of the results from Stauffer et al. (1985), Stauffer, Hartmann & Jones (1989), Prosser et al. (1993a), Prosser (1991), Prosser et al. (1993b), O’Dell & Collier Cameron (1993), Prosser et al. (1995), O’Dell, Hendry & Collier Cameron (1994), O’Dell et al. (1996), Allain et al. (1996), Martín & Zapatero Osorio (1997), Prosser & Randich (1998), Prosser, Randich & Simon (1998), Barnes et al. (1998), and the Hyades data from Radick et al. (1987) and Prosser et al. (1995), taken from the open cluster data base. The solid lines show the predicted evolution from equations (10) and (11) for a $0.8 M_{\odot}$ star in the left-hand panel, and a $0.6 M_{\odot}$ star in the right-hand panel. The dashed lines show only the $t^{1/2}$ angular momentum loss component from (11) for comparison.

Bouvier 1997 and Keppens, MacGregor & Charbonneau 1995) cause much less efficient braking on the ZAMS for the first few hundred Myr, giving rise to faster rotators at the age of M34 than we have detected for these masses.

6 CONCLUSIONS

We have reported on results of a photometric survey of M34 in V and i bands. Selection of candidate members in a V versus $V - I$ CMD using an empirical fit to the cluster main sequence found 714 candidate members, over a V magnitude range of $14 < V < 24$ ($0.12 \lesssim M/M_{\odot} \lesssim 1.0$). The likely field contamination level was estimated using a simulated catalogue of field objects from the Besançon galactic models (Robin et al. 2003), finding that ~ 283 objects were likely field contaminants, an overall contamination level of ~ 39 per cent, implying that there are ~ 400 real cluster members over this mass range in our FOV. The next step in our membership survey will be to combine our optical data with planned near-IR photometry and optical spectroscopy to reduce the contamination level.

The M34 mass function was examined over the range $0.1 \lesssim M/M_{\odot} \lesssim 1.0$ ($13 < I < 20$), finding that a lognormal function was a good description of the data in $dN/d \log M$, with parameters $M_0 = 0.44 \pm 0.31 M_{\odot}$ (the mass at maximum dN/dM), and $\sigma = 0.66 \pm 0.08$.

From ~ 8 nights of time-series photometry (many of which were partial) we derived light curves for ~ 8500 objects in the M34 field, achieving a precision of < 1 per cent over $13 \lesssim i \lesssim 17$. The light curves of our candidate M34 cluster members were searched for periodic variability corresponding to stellar rotation, giving 105 detections over the mass range $0.25 < M/M_{\odot} < 1.0$.

The rotational period distribution for $0.4 < M/M_{\odot} < 1.0$ was found to peak at ~ 7 d with a tail of fast rotators having rotational

periods down to ~ 0.8 d. Our data suggest that most of the angular momentum loss for stars with masses $\gtrsim 0.4 M_{\odot}$ happens on the early main sequence, by the age of M34 (~ 200 Myr), in particular for the slow rotators. We observed a number of rapidly rotating stars ($v_{\text{rot}} \sim 50\text{--}100 \text{ km s}^{-1}$), finding in general that the results can be explained by models of stellar angular momentum loss assuming solid body rotation (e.g. Bouvier et al. 1997) without needing to invoke core–envelope decoupling, which seems to give rise to faster rotators at the age of M34 than we have detected for these masses.

Our rotation period distribution for $0.25 < M/M_{\odot} < 0.4$ was found to peak at short periods, with a lack of slow rotators (e.g. $P \gtrsim 5$ d). Our simulations indicate that the effect is real and does not result from a biased sample. This is consistent with the work of other authors (e.g. Scholz & Eislöffel 2004) at very low masses.

The multiband photometry we have obtained can be used to examine the properties of the star spots giving rise to the rotational modulations. This will be investigated in a future publication.

One of the major problems in our survey is field contamination. We intend to publish the final catalogue of M34 membership candidates after obtaining follow-up spectroscopy. However, the preliminary catalogue of membership candidates is available on request.

ACKNOWLEDGMENTS

The INT is operated on the island of La Palma by the Isaac Newton Group in the Spanish Observatorio del Roque de los Muchachos of the Instituto de Astrofísica de Canarias. This publication makes use of data products from the 2MASS, which is a joint project of the University of Massachusetts and the Infrared Processing and Analysis Center/California Institute of Technology, funded by the National Aeronautics and Space Administration and the National Science Foundation. This research has also

made use of the SIMBAD data base, operated at CDS, Strasbourg, France. The Open Cluster Database, as provided by C. F. Prosser (deceased) and J. R. Stauffer, may currently be accessed at <http://www.noao.edu/noao/staff/cprosser/>, or by anonymous ftp to 140.252.1.11, <cd/pub/prosser/clusters/>.

JI gratefully acknowledges the support of a PPARC studentship, and SA the support of a PPARC postdoctoral fellowship. We also thank Alexander Scholz for his assistance during SA's trip to Toronto, and the anonymous referee for valuable comments which helped to improve the paper.

REFERENCES

- Allain S., 1998, *A&A*, 333, 629
 Allain S., Fernandez M., Martín E. L., Bouvier J., 1996, *A&A*, 314, 173
 Baraffe I., Chabrier G., Allard F., Hauschildt P. H., 1998, *A&A*, 337, 403
 Barnes J. R., Collier Cameron A., Unruh Y. C., Donati J. F., Hussain G. A. J., 1998, *MNRAS*, 299, 904
 Barnes S., Sofia S., 1996, *ApJ*, 462, 746
 Barnes S. A., 2003, *ApJ*, 586, 464
 Barnes S. A., Sofia S., Prosser C. F., Stauffer J. R., 1999, *ApJ*, 516, 263
 Barrado y Navascués D., Stauffer J. R., Jayawardhana R., 2004, *ApJ*, 614, 386
 Bouvier J., 1997, *Mem. Soc. Astron. Ital.*, 68, 881
 Bouvier J., Forestini M., Allain S., 1997, *A&A*, 326, 1023
 Canterna R., Crawford D. L., Perry C. L., 1979, *PASP*, 91, 263
 Collier Cameron A., Campbell C. G., Quaintrell H., 1995, *A&A*, 298, 133
 Eff-Darwich A., Korzennik S. G., Jiménez-Reyes S. J., 2002, *ApJ*, 573, 857
 Elias J. H., Frogel J. A., Matthews K., Neugebauer G., 1982, *AJ*, 87, 1029
 Elias J. H., Frogel J. A., Hyland A. R., Jones T. J., 1983, *AJ*, 88, 1027
 Giampapa M. S., Rosner R., Kashyap V., Fleming T. A., Schmitt J. H. M. M., Bookbinder J. A., 1996, *ApJ*, 463, 707
 Haisch K. E. Jr, Lada E. A., Lada C. J., 2001, *ApJ*, 553, 153
 Herbst W., Bailer-Jones C. A. L., Mundt R., Meisenheimer K., Wackermann R., 2002, *A&A*, 396, 513
 Hillenbrand L., 1997, *AJ*, 113, 1733
 Hodgkin S. T., Irwin J. M., Aigrain S., Hebb L., Moraux E., Irwin M. J., 2006, *AN*, 327, 9
 Ianna P. A., Schlemmer D. M., 1993, *AJ*, 105, 209
 Irwin M. J., Lewis J. R., 2001, *New Astron. Rev.*, 45, 105
 Jeffries R. D., Thurston M. R., Hambly N. C., 2001, *A&A*, 375, 863
 Jones B. F., Prosser C. F., 1996, *AJ*, 111, 1193
 Kalirai J. S., Fahlman G. G., Richer H. B., Ventura P., 2003, *AJ*, 126, 1402
 Keppens R., MacGregor K. B., Charbonneau P., 1995, *A&A*, 294, 469
 Konacki M., Torres G., Jha S., Sasselov D. D., 2003, *Nat*, 421, 507
 Königl A., 1991, *ApJ*, 370, L37
 Krishnamurthi A., Pinsonneault M. H., Barnes S., Sofia S., 1997, *ApJ*, 480, 303
 Krishnamurthi et al., 1998, *ApJ*, 493, 914
 Landolt A. J., 1992, *AJ*, 104, L340
 Leggett S. K., 1992, *ApJS*, 82, 351
 Magnitskii A. K., 1987, *Sov. Astron. Lett.*, 13, 451
 Martín E. L., Zapatero Osorio M. R., 1997, *MNRAS*, 286, L17
 Meynet G., Mermillod J.-C., Maeder A., 1993, *A&AS*, 98, 477
 Moitinho A., Alves J., Huéramo N., Lada C. J., 2001, *ApJ*, 563, 73
 Moraux E., Bouvier J., Clarke C., 2005, *Mem. Soc. Astron. Ital.*, 76, 265
 O'Dell M. A., Collier Cameron A., 1993, *MNRAS*, 262, 521
 O'Dell M. A., Hendry M. A., Collier Cameron A., 1994, *MNRAS*, 268, 181
 O'Dell M. A., Hilditch R. W., Collier Cameron A., Bell S. A., 1996, *MNRAS*, 284, 874
 Patten B. M., Simon T., 1996, *ApJS*, 106, 489
 Perryman M. A. C. et al., 1998, *A&A*, 331, 81
 Prosser C. F., 1991, PhD thesis, Univ. California, Santa Cruz
 Prosser C. F., Randich S., Simon T., 1998, *AN*, 319, 215
 Prosser C. F., Schild R. E., Stauffer J. R., Jones B. F., 1993a, *PASP*, 105, 269
 Prosser C. F. et al., 1993b, *PASP*, 105, 1407
 Prosser C. F. et al., 1995, *PASP*, 107, 211
 Prosser C. F., Randich S., 1998, *AN*, 319, 210
 Radick R. R., Thompson D. T., Lockwood G. W., Duncan D. K., Baggett W. E., 1987, *ApJ*, 321, 459
 Rebull L. M., Stauffer J. R., Megeath S. T., Hora J. L., Hartmann L., 2006, *ApJ*, in press, preprint (astro-ph/0604104)
 Reid I. N., Gizis J. E., Hawley S. L., 2002, *AJ*, 124, 2721
 Robin A. C., Reylé C., Derrière S., Picaud S., 2003, *A&A*, 409, 523
 Scholz A., Eislöffel J., 2004, *A&A*, 421, 259
 Schuler S. C., King J. R., Fischer D. A., Soderblom D. R., Jones B. F., 2003, *AJ*, 125, 2085
 Simon T., 2000, *PASP*, 112, 599
 Skumanich A., 1972, *ApJ*, 171, 565
 Soderblom D. R., Stauffer J. R., Hudon J. D., Jones B. F., 1993a, *ApJS*, 85, 315
 Soderblom D. R., Stauffer J. R., MacGregor K. B., Jones B. F., 1993b, *ApJ*, 409, 624
 Soderblom D. R., Jones B. F., Fischer D., 2001, *ApJ*, 563, 334
 Stassun K. G., Terndrup D., 2003, *PASP*, 115, 505
 Stassun K. G., Mathieu R. D., Mazeh T., Vrba F. J., 1999, *AJ*, 117, 2941
 Stauffer J. R., Hartmann L. W., Burnham J. N., Jones B. F., 1985, *ApJ*, 289, 247
 Stauffer J. R., Schild R. A., Baliunas S. L., Africano J. L., 1987, *PASP*, 99, 471
 Stauffer J. R., Hartmann L. W., Jones B. F., 1989, *ApJ*, 346, 160
 Stauffer J. R., Schultz G., Kirkpatrick J. D., 1998, *ApJ*, 499, 199
 Stauffer J. R. et al., 1999, *ApJ*, 527, 219
 Terndrup D. M., Krishnamurthi A., Pinsonneault M. H., Stauffer J. R., 1999, *AJ*, 118, 1814
 Van Leeuwen F., Alphenaar P., Meys J. J. M., 1987, *A&AS*, 67, 483
 Weber E. J., Davis L., Jr, 1967, *ApJ*, 148, 217

APPENDIX A: LIGHT CURVES AND TABULAR DATA

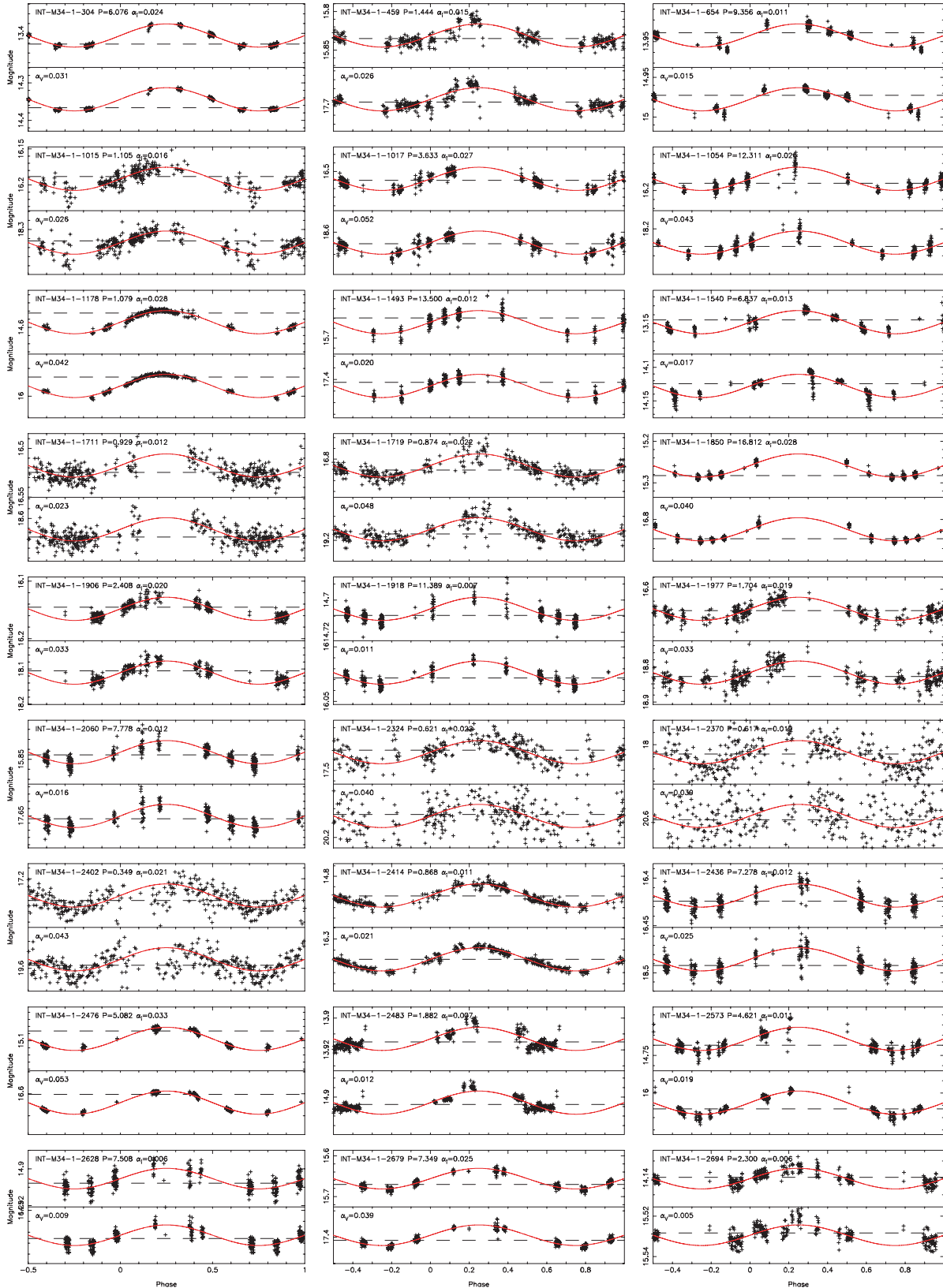


Figure A1. Phase-folded light curves of our 105 periodic variables classified as candidate cluster members. The upper panel for each object shows the *i*-band light curve, the lower panel the *V*-band light curve. The dashed lines show the median flux level of the object, and the solid lines show the fitted sine curves. The light curves are labelled with period P in d, and α_i and α_V , the amplitudes in *i* and *V* bands, respectively. See also Table A1.

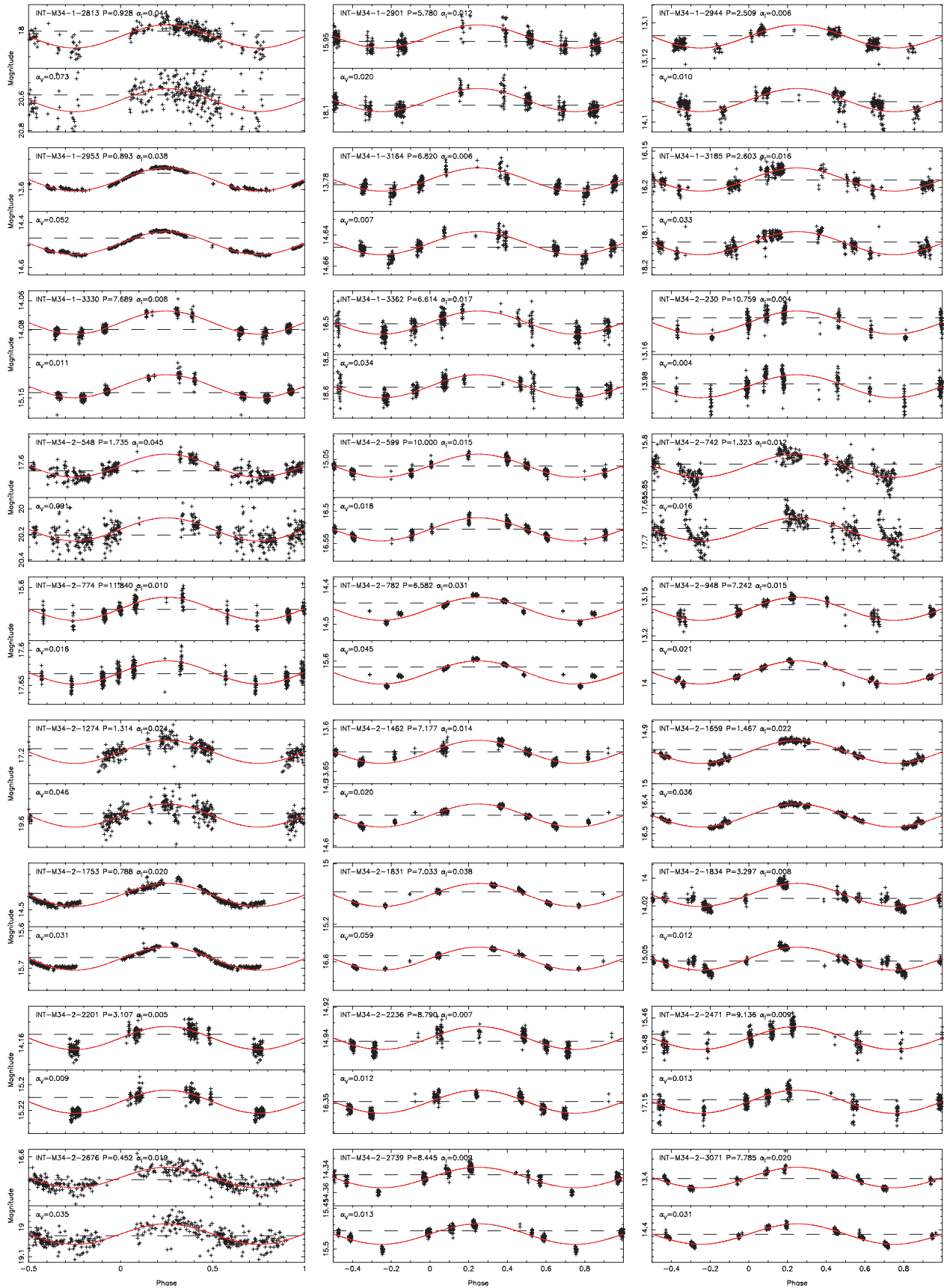


Figure A1 – continued

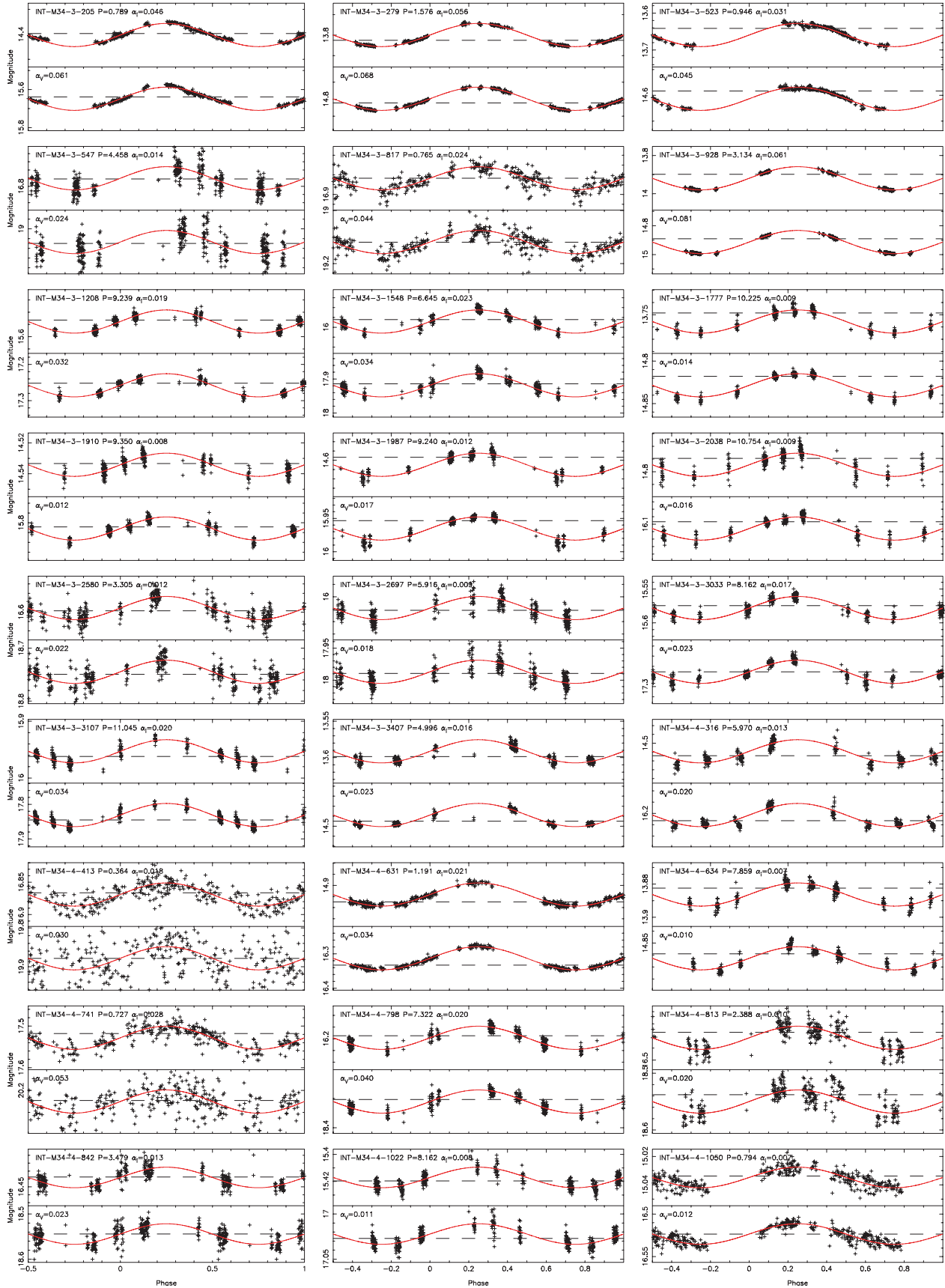


Figure A1 – continued

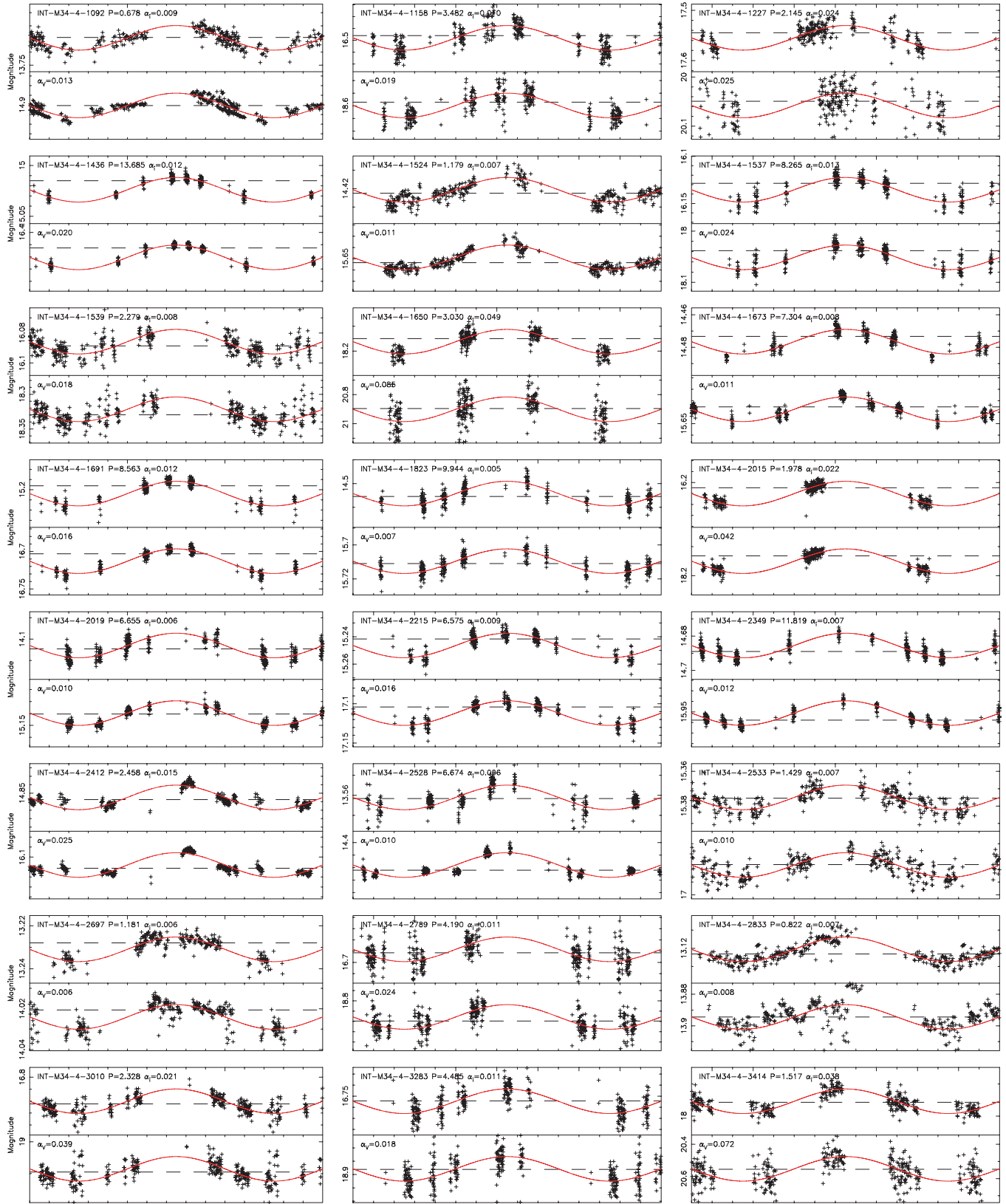


Figure A1 – continued

Table A1. Summary of the properties of our 105 M34 rotation candidates. The period P in d, and amplitudes α_V and α_i in the V and i bands (units of magnitudes, in the instrumental bandpass), interpolated mass and radius (from the models of Baraffe et al. 1998, derived using the I magnitudes), identification number of Jones & Prosser (1996), and $v \sin i$ measurements of Soderblom et al. (2001) are given (where available). The following flags are used as superscripts to the period: ‘ a ’ indicating cases where the period was ambiguous (with both long and short periods fitting equally well to the observations), ‘ b ’ indicating a poorly constrained long period (due to the short observing window) and ‘ c ’ indicating objects where the V -band detection was saturated, so the i band only was used to fit the period (NB: the V -band magnitudes and amplitudes are unreliable for these objects).

Identifier	Right ascension (RA) (J2000)	Declination (Dec.) (J2000)	V (mag)	R (mag)	I (mag)	$H\alpha$ (mag)	P (d)	α_V (mag)	α_i (mag)	M (M_\odot)	R (R_\odot)	JP	$v \sin i$ (km s^{-1})
M34-1-304	02 42 56.88	+42 35 22.0	14.52	13.20	13.50	13.91	6.076	0.031	0.024	0.90	0.87	522	
M34-1-459	02 42 51.73	+42 33 48.9	17.84	16.74	15.79	16.59	1.444	0.026	0.015	0.58	0.54		
M34-1-654	02 42 46.41	+42 39 11.4	15.12	13.90	14.00	14.44	9.356	0.015	0.011	0.82	0.77	487	
M34-1-1015	02 42 34.26	+42 31 00.5	18.47	17.34	16.16	17.14	1.105 ^a	0.026	0.016	0.53	0.49		
M34-1-1017	02 42 35.02	+42 39 29.0	18.81	17.63	16.46	17.42	3.633	0.052	0.027	0.49	0.45		
M34-1-1054	02 42 33.07	+42 30 02.0	18.43	17.28	16.15	17.07	12.311 ^b	0.043	0.026	0.53	0.49		
M34-1-1178	02 42 31.54	+42 37 10.5	16.08	15.04	14.58	15.19	1.079	0.042	0.028	0.74	0.69	424	23.3
M34-1-1493	02 42 23.32	+42 38 21.0	17.56	16.48	15.65	16.41	13.500 ^b	0.020	0.012	0.60	0.56		
M34-1-1540	02 42 21.89	+42 32 13.1	14.27	12.83	13.20	13.63	6.837	0.017	0.013	0.95	0.92	377	11.1
M34-1-1711	02 42 16.99	+42 38 12.0	18.79	17.59	16.45	17.42	0.929 ^a	0.023	0.012	0.49	0.45		
M34-1-1719	02 42 16.16	+42 34 01.0	19.32	18.03	16.72	17.82	0.874	0.048	0.022	0.45	0.41		
M34-1-1850	02 42 11.67	+42 31 17.9	17.01	15.95	15.28	15.92	16.812 ^b	0.040	0.028	0.65	0.61		
M34-1-1906	02 42 10.65	+42 34 09.1	18.25	17.11	16.09	16.97	2.408	0.033	0.020	0.54	0.50		
M34-1-1918	02 42 10.30	+42 34 50.2	16.18	15.13	14.73	15.28	11.389 ^b	0.011	0.007	0.72	0.67		
M34-1-1977	02 42 07.85	+42 37 45.1	18.97	17.77	16.55	17.56	1.704	0.033	0.019	0.47	0.43		
M34-1-2060	02 42 04.92	+42 37 47.3	17.80	16.69	15.81	16.60	7.778	0.016	0.012	0.58	0.54		
M34-1-2324	02 41 55.85	+42 33 32.5	20.26	18.86	17.32	18.62	0.621	0.040	0.022	0.36	0.34		
M34-1-2370	02 41 54.69	+42 35 29.7	20.73	19.41	17.88	19.12	0.617	0.039	0.019	0.28	0.28		
M34-1-2402	02 41 53.31	+42 32 10.0	19.70	18.49	17.16	18.23	0.349	0.043	0.021	0.38	0.35		
M34-1-2414	02 41 53.25	+42 35 26.3	16.48	15.53	14.82	15.49	0.868	0.021	0.011	0.70	0.66		
M34-1-2436	02 41 52.59	+42 36 01.6	18.63	17.47	16.36	17.30	7.278	0.025	0.012	0.50	0.46		
M34-1-2476	02 41 51.70	+42 38 23.4	16.75	15.85	15.08	15.75	5.082	0.053	0.033	0.67	0.63		
M34-1-2483	02 41 51.31	+42 34 24.8	15.06	13.67	13.98	14.40	1.882	0.012	0.007	0.82	0.78	241	
M34-1-2573	02 41 48.98	+42 39 59.7	16.18	15.25	14.75	15.31	4.621	0.019	0.011	0.71	0.67		
M34-1-2628	02 41 46.37	+42 32 31.9	16.43	15.50	14.93	15.49	7.508	0.009	0.006	0.69	0.65		
M34-1-2679	02 41 44.20	+42 35 35.9	17.56	16.48	15.65	16.39	7.349	0.039	0.025	0.60	0.56		
M34-1-2694	02 41 43.96	+42 40 31.7	15.68	14.61	14.15	14.73	2.300	0.005	0.006	0.80	0.75	198	
M34-1-2813	02 41 39.72	+42 38 06.7	20.70	19.38	17.88	19.09	0.928	0.073	0.044	0.28	0.28		
M34-1-2901	02 41 36.60	+42 40 03.9	18.24	17.02	15.87	16.88	5.780	0.020	0.012	0.57	0.53		
M34-1-2944	02 41 35.08	+42 33 30.9	14.23	12.80	13.18	13.59	2.509 ^c	0.010	0.006	0.96	0.93	159	
M34-1-2953	02 41 35.25	+42 41 02.5	14.63	13.62	13.62	14.05	0.893	0.052	0.038	0.88	0.85	158	45.0
M34-1-3164	02 41 27.66	+42 35 42.1	14.79	13.46	13.85	14.23	6.820	0.007	0.006	0.84	0.80	131	
M34-1-3185	02 41 26.29	+42 30 14.9	18.28	17.13	16.13	17.00	2.603	0.033	0.016	0.53	0.49		
M34-1-3330	02 41 21.40	+42 35 44.4	15.29	14.03	14.15	14.59	7.689	0.011	0.008	0.80	0.75	105	
M34-1-3362	02 41 20.03	+42 39 23.7	18.74	17.56	16.44	17.38	6.614	0.034	0.017	0.49	0.45		
M34-2-230	02 40 30.63	+42 51 01.5	14.16	13.24	13.25	13.63	10.759 ^b	0.004	0.004	0.94	0.91		
M34-2-548	02 40 09.57	+42 48 37.3	20.37	18.99	17.52	18.76	1.735	0.091	0.045	0.33	0.32		
M34-2-599	02 40 49.09	+42 48 20.4	16.69	15.71	15.06	15.69	10.000	0.018	0.015	0.67	0.63		
M34-2-742	02 40 15.08	+42 47 13.6	17.88	16.73	15.79	16.62	1.323	0.016	0.012	0.58	0.54		
M34-2-774	02 40 24.27	+42 46 57.1	17.82	16.62	15.58	16.52	11.840 ^b	0.016	0.010	0.61	0.57		
M34-2-782	02 40 49.66	+42 46 55.0	15.79	15.03	14.47	15.00	6.582	0.045	0.031	0.75	0.70	18	
M34-2-948	02 40 26.58	+42 45 40.0	14.16	13.23	13.24	13.61	7.242	0.021	0.015	0.95	0.92		
M34-2-1274	02 40 38.20	+42 43 06.6	19.71	18.48	17.08	18.20	1.314	0.046	0.024	0.40	0.36		
M34-2-1462	02 40 30.38	+42 41 51.8	14.72	13.61	13.68	14.11	7.177	0.020	0.014	0.87	0.83		
M34-2-1659	02 40 26.71	+42 40 15.6	16.62	15.66	14.95	15.60	1.467	0.036	0.022	0.69	0.65		
M34-2-1753	02 40 48.54	+42 39 25.7	15.82	14.99	14.49	15.02	0.788	0.031	0.020	0.75	0.70		
M34-2-1831	02 40 42.78	+42 38 59.1	16.74	15.74	15.09	15.74	7.033	0.059	0.038	0.67	0.63		
M34-2-1834	02 40 05.98	+42 38 57.4	15.22	14.25	14.08	14.51	3.297	0.012	0.008	0.81	0.76		
M34-2-2201	02 40 30.81	+42 36 25.0	15.38	14.38	14.21	14.65	3.107	0.009	0.005	0.79	0.74		
M34-2-2236	02 40 19.31	+42 36 12.9	16.51	15.56	14.96	15.53	8.790	0.012	0.007	0.69	0.65		
M34-2-2471	02 40 57.86	+42 34 39.3	17.30	16.23	15.44	16.17	9.136	0.013	0.009	0.62	0.58		
M34-2-2676	02 40 53.92	+42 33 16.5	19.18	17.95	16.54	17.66	0.452	0.035	0.019	0.47	0.43		

Table A1 – continued

Identifier	RA (J2000)	Dec. (J2000)	<i>V</i> (mag)	<i>R</i> (mag)	<i>I</i> (mag)	H α (mag)	<i>P</i> (d)	α_V (mag)	α_i (mag)	<i>M</i> (M_{\odot})	<i>R</i> (R_{\odot})	JP	<i>v</i> sin <i>i</i> (km s ⁻¹)
M34-2-2739	02 40 33.29	+42 32 54.3	15.64	14.76	14.38	14.84	8.445 ^a	0.013	0.009	0.76	0.71		
M34-2-3071	02 40 48.91	+42 30 34.1	14.60	13.51	13.45	13.88	7.785	0.031	0.020	0.91	0.88		
M34-3-205	02 42 59.94	+42 58 01.5	15.81	14.64	14.44	14.94	0.789	0.061	0.046	0.76	0.71	536	44.0
M34-3-279	02 42 57.82	+42 58 03.8	14.97	13.67	13.87	14.25	1.576	0.068	0.056	0.84	0.80	524	
M34-3-523	02 42 50.76	+42 58 07.8	14.75	13.58	13.71	14.09	0.946	0.045	0.031	0.86	0.83	499	
M34-3-547	02 42 49.81	+43 00 35.3	19.20	17.97	16.72	17.74	4.458	0.024	0.014	0.45	0.41		
M34-3-817	02 42 39.42	+42 55 27.7	19.30	18.06	16.78	17.83	0.765	0.044	0.024	0.44	0.40		
M34-3-928	02 42 36.30	+42 54 31.4	15.07	13.73	13.98	14.41	3.134	0.081	0.061	0.82	0.78	444	
M34-3-1208	02 42 24.90	+42 53 25.9	17.43	16.39	15.55	16.25	9.239	0.032	0.019	0.61	0.57		
M34-3-1548	02 42 10.29	+42 59 35.9	18.08	16.90	15.94	16.80	6.645	0.034	0.023	0.56	0.52		
M34-3-1777	02 42 02.26	+43 01 13.3	15.01	13.45	13.82	14.25	10.225 ^b	0.014	0.009	0.85	0.81	288	7.0
M34-3-1910	02 41 57.92	+42 53 22.4	15.97	14.71	14.56	15.09	9.350 ^a	0.012	0.008	0.74	0.69	268	7.0
M34-3-1987	02 41 55.95	+42 58 30.8	16.17	14.71	14.69	15.24	9.240 ^a	0.017	0.012	0.72	0.68		
M34-3-2038	02 41 54.26	+42 59 35.6	16.29	15.01	14.82	15.36	10.754 ^a	0.016	0.009	0.70	0.66	253	
M34-3-2580	02 41 36.18	+42 54 55.7	18.91	17.70	16.52	17.51	3.305	0.022	0.012	0.48	0.44		
M34-3-2697	02 41 32.72	+43 02 16.3	18.17	16.98	15.98	16.85	5.916	0.018	0.009	0.55	0.51		
M34-3-3033	02 41 18.44	+42 58 21.3	17.45	16.34	15.55	16.27	8.162	0.023	0.017	0.61	0.57		
M34-3-3107	02 41 20.45	+42 58 52.3	18.02	16.76	15.95	16.75	11.045 ^b	0.034	0.020	0.56	0.52		
M34-3-3407	02 41 05.13	+42 56 43.1	14.65	13.46	13.67	14.00	4.996	0.023	0.016	0.87	0.84	49	
M34-4-316	02 42 57.86	+42 41 46.7	16.35	15.22	14.49	15.19	5.970	0.020	0.013	0.75	0.70	527	
M34-4-413	02 42 55.14	+42 50 40.8	20.01	18.57	16.69	18.24	0.364	0.030	0.018	0.45	0.41		
M34-4-631	02 42 47.53	+42 45 46.8	16.47	15.52	14.94	15.53	1.191	0.034	0.021	0.69	0.65		
M34-4-634	02 42 47.72	+42 47 42.9	15.00	13.97	13.94	14.34	7.859	0.010	0.007	0.83	0.79	489	7.8
M34-4-741	02 42 43.65	+42 45 41.8	20.37	19.07	17.38	18.68	0.727	0.053	0.028	0.35	0.33		
M34-4-798	02 42 41.81	+42 46 01.8	18.44	17.26	16.12	17.10	7.322	0.040	0.020	0.53	0.49		
M34-4-813	02 42 41.06	+42 44 22.2	18.69	17.53	16.42	17.34	2.388	0.020	0.010	0.49	0.45		
M34-4-842	02 42 40.62	+42 48 55.6	18.69	17.52	16.37	17.31	3.479	0.023	0.013	0.50	0.46		
M34-4-1022	02 42 33.96	+42 43 26.2	17.17	16.08	15.41	16.07	8.162	0.011	0.008	0.63	0.59		
M34-4-1050	02 42 33.61	+42 49 12.2	16.66		15.03	15.66	0.794	0.012	0.007	0.68	0.64		
M34-4-1092	02 42 32.28	+42 49 05.9	15.05	13.87	13.76	14.25	0.678	0.013	0.009	0.86	0.82	425	17.3
M34-4-1158	02 42 28.95	+42 42 10.5	18.74	17.57	16.42	17.37	3.482	0.019	0.010	0.49	0.45		
M34-4-1227	02 42 26.30	+42 43 15.9	20.18	18.88	17.42	18.63	2.145	0.025	0.024	0.34	0.33		
M34-4-1436	02 42 20.30	+42 49 05.5	16.57	15.61	15.02	15.60	13.685 ^b	0.020	0.012	0.68	0.64		
M34-4-1524	02 42 17.23	+42 48 18.6	15.80	14.95	14.45	14.97	1.179	0.011	0.007	0.75	0.70	356	15.4
M34-4-1537	02 42 16.19	+42 43 11.3	18.17	17.07	16.07	16.92	8.265 ^b	0.024	0.013	0.54	0.50		
M34-4-1539	02 42 17.30	+42 51 29.8	18.47	17.25	16.00	17.03	2.279	0.018	0.008	0.55	0.51		
M34-4-1650	02 42 12.54	+42 49 28.5	21.00	19.62	18.00	19.35	3.030	0.085	0.049	0.26	0.27		
M34-4-1673	02 42 11.71	+42 43 48.2	15.77	14.93	14.51	14.98	7.304	0.011	0.008	0.75	0.70	330	
M34-4-1691	02 42 10.99	+42 43 16.3	16.84	15.87	15.18	15.82	8.563	0.016	0.012	0.66	0.62		
M34-4-1823	02 42 07.50	+42 47 26.7	15.85		14.53	15.03	9.944	0.007	0.005	0.74	0.69	310	
M34-4-2015	02 42 01.81	+42 41 58.9	18.27		16.14	16.99	1.978	0.042	0.022	0.53	0.49		
M34-4-2019	02 42 02.55	+42 51 51.4	15.30	14.41	14.17	14.59	6.655	0.010	0.006	0.79	0.74	289	7.4
M34-4-2215	02 41 55.25	+42 50 31.7	17.24	16.14	15.20	16.02	6.575 ^a	0.016	0.009	0.66	0.62		
M34-4-2349	02 41 50.31	+42 44 37.6	16.09		14.72	15.22	11.819 ^a	0.012	0.007	0.72	0.67	229	8.2
M34-4-2412	02 41 48.48	+42 49 33.6	16.27	15.41	14.88	15.43	2.458	0.025	0.015	0.70	0.66	218	
M34-4-2528	02 41 44.17	+42 46 07.5	14.56		13.62	13.97	6.674	0.010	0.006	0.88	0.85	199	9.5
M34-4-2533	02 41 43.86	+42 45 08.1	17.10	16.13	15.37	16.03	1.429	0.010	0.007	0.63	0.59		
M34-4-2697	02 41 38.14	+42 44 04.4	14.15	13.30	13.30	13.64	1.181 ^c	0.006	0.006	0.93	0.90	177	
M34-4-2789	02 41 34.88	+42 48 52.7	18.98	17.75	16.62	17.61	4.190 ^a	0.024	0.011	0.46	0.42		
M34-4-2833	02 41 33.43	+42 42 11.8	14.04		13.20	13.54	0.822 ^c	0.008	0.007	0.95	0.92	148	
M34-4-3010	02 41 26.73	+42 51 34.1	19.24	18.04	16.75	17.81	2.328	0.039	0.021	0.44	0.40		
M34-4-3283	02 41 16.53	+42 49 34.8	19.04	17.85	16.67	17.66	4.485	0.018	0.011	0.45	0.41		
M34-4-3414	02 41 11.55	+42 46 22.4	20.66	19.37	17.81	19.08	1.517	0.072	0.038	0.29	0.29		

This paper has been typeset from a $\text{\TeX}/\text{\LaTeX}$ file prepared by the author.